Plasma Sources Science and Technology

PAPER

Electron swarm and streamer transport across the gas–liquid interface: a comparative fluid model study

To cite this article: N A Garland *et al* 2018 *Plasma Sources Sci. Technol.* **27** 105004

View the article online for updates and enhancements.

IOP ebooks™

Bringing you innovative digital publishing with leading voices to create your essential collection of books in STEM research.

Start exploring the collection - download the first chapter of every title for free.

This content was downloaded from IP address 129.108.9.184 on 19/10/2018 at 23:18

IOP Publishing Plasma Sources Science and Technology
Plasma Sources Sci. Technol. **27** (2018) 105004 (21pp) https://doi.org/10.1088/1361-6595/aae05c

Electron swarm and streamer transport across the gas–liquid interface: a comparative fluid model study

N A Garland[1], I Simonović[2], G J Boyle[1,3], D G Cocks[4], S Dujko[2] and R D White[1]

[1] College of Science and Engineering, James Cook University, Townsville, QLD 4811, Australia
[2] Institute of Physics, University of Belgrade, Pregrevica 118, 11080 Belgrade, Serbia
[3] Deutsches Elektronen-Synchrotron DESY, Hamburg, Germany
[4] Plasma Research Laboratories, Australian National University, Canberra, 2601, ACT, Australia

E-mail: nathan.garland@my.jcu.edu.au

Received 29 April 2018, revised 5 September 2018
Accepted for publication 11 September 2018
Published 15 October 2018

Abstract

In this work we present a comparative study of fluid modeling methods in order to determine a recommended procedure to describe electron transport and streamer propagation across gas–liquid interfacial regions. A test case of a cryogenic argon gas–liquid interface is simulated in this work to demonstrate applicability of the recommended procedures. The recommended non-local four moment model takes into consideration the density variation across the interface, and its associated impact on the transport properties/collisional transfer rates, as well as the spatial variation of the dielectric permittivity and the conduction band through the liquid binding energy, V_0. The study examines the impacts of various assumptions involved in the modeling of electron transport across the plasma-liquid interface, by comparing a local field (drift-diffusion) approximation with the non-local (four moment) model, as well as a step function change in the density to actual spatially dependent density variations across the interface. We provide recommendations on necessary physical considerations needed to adequately model transport phenomena across gas–liquid interfaces.

Keywords: electron transport, gas liquid interface, fluid model, streamer, ionization front, low temperature plasma

1. Introduction

Over the last century, there has been much effort applied to furthering the understanding of plasma discharges in gases, and developing advanced predictive models for both industrial applications, including microelectronic circuit manufacture [1–3], and for understanding complex natural phenomena such as lightning [4–6]. In addition to gas discharges, there is increasing interest in modeling discharges in liquids [7, 8] to better understand processes such as underwater arc welding and plasma medicine [9–12]. At the nexus of these two extremes is the gas–liquid interface, which has been of particular interest to the plasma community due to emerging applications such as plasma medicine. While advanced models for gas discharges, and recently liquid discharges, are available [13–15] we believe there is an opportunity to unify the two extremes in order to model electron transport as a continuous process between gas and liquid. In this study we present the framework, and application, of such a model to electron transport across an argon gas–liquid interface.

Argon was chosen as the background medium for this study primarily because much work has already been done to understand electron transport in both gaseous and, recently, liquid argon [16, 17] and so the input data required for fluid models was readily available. In addition to the availability of input data, the study of electron transport over argon gas–liquid interfaces is directly applicable to the field of dual-phase particle detectors used to detect dark matter or neutrino scattering events [18–22]. In these experiments a very small

 © 2018 IOP Publishing Ltd

reduced electric field $\approx 10^{-2}$–10^{-1} Td, where 1 Td $= 10^{-21}$ V m^2, is applied to a large volume of cryogenic liquid argon, or xenon, to assist in extracting electrons produced by ionization events in the liquid [22]. These electrons are extracted through the surface of the liquid, where they transport across an interface into a vapor region atop the liquid. Once in the gas phase, the current produced by the extracted electrons is amplified by multiplier grids providing stronger reduced electric fields ($\approx 10^2$ Td) to generate avalanche events. We identify this application as one that could benefit from a modeling framework that could provide a continuous simulation of electron transport out of the liquid, across the interface, and into the gas phase.

Conversely, in terms of plasma transport from gas phase to liquid, a major application is plasma medicine and plasma treatment of liquids. The importance of electron transfer and electron induced chemistry at these plasma-liquid interfaces has been well established in recent years [11, 12, 23]. Despite this importance, it has been noted that radicals, ions, and photons are primarily considered when studying plasma-liquid reactions with little attention given to electron interactions with the liquid phase [11]. We note that this present study focuses on electron transport in argon, a non-polar atomic fluid that is relatively simple when compared to complex biological tissue or even water. Despite this, we believe the methodology and framework presented in this study presents an important first step towards simulating more complicated plasma-liquid interactions.

In order to model charged particle transport between gas and liquid media, a range of methods have been used in the literature. Some studies have modeled charged particle transport in gases and liquids as two separate models, each including distinctly different physics, coupled by matching conditions at the boundary [9, 24–27]. Alternatively, liquid interface effects have been simply treated as a density and energy absorption or emission boundary condition applied to a single gas phase model [10, 24, 27]. Finally, we note that there is an obvious temptation to simply use existing gas phase transport models and input data, and 'scale-up' the input data to liquid neutral densities in order to simulate transport in liquids [24, 28]. The errors in this assumption have been addressed in previous studies [16, 17, 29, 30], and in this study we demonstrate how to better accommodate transport in liquids through accurate input data.

The aims of this comparative study were to extend a recently proposed and benchmarked higher order four moment fluid model [13], as well as drift diffusion fluid models [4, 14, 15, 31, 32], to simulate electron transport across gas–liquid interfaces and formulate a recommendation for best practice future interfacial modeling. Interfacial considerations will be addressed by comparing the types of fluid model used but also through comparison of functional form assumptions for neutral density, n_0, variation of the interface. Inclusion of gas–liquid interface effects, such as variation of delocalized electron energy level, V_0, and dielectric permittivity, ε, into the proposed modeling framework will also be addressed.

We begin this study by briefly reviewing fluid models used for electron transport in gases and liquids in section 2 where distinctions between gas and liquid phase electron transport are highlighted. In section 3 a continuous fluid model of electron transport between gas and liquid media is proposed, with modifications to include some interfacial effects discussed. The results of the proposed interfacial fluid models are detailed in section 4, with key advantages and disadvantages of each model highlighted, with details of the numerical solution method employed in this study available in appendix B. Finally, in section 5, key recommendations drawn from the results of this study are made, with a focus on how to best accommodate interfacial electron transport in future fluid models.

2. Fluid modeling in gases and liquids

2.1. Fluid models for electron transport

Fluid models have been used to describe plasma phenomena such as streamers [4, 15, 33], industrial plasmas used in fabricating microelectronics [2, 34], and more recently biomedical [23, 24] applications of discharges. Fluid models are essentially continuity equations of velocity-averaged, spatially varying macroscopic variables, such as particle density, momentum, and energy [4, 13–15, 31] derived via velocity moments of the Boltzmann equation [13, 35]. This gives a relatively straightforward macroscopic model that provides a good description of the discharge dynamics, without the computational overhead of comprehensive particle based methods. Error bounds of fluid models are considered to be within 10%–20% [36], and are suited to providing a 'line-of-best-fit' description of charged particle properties, especially when non-trivial electron velocity distributions are present [13].

Advanced solution techniques, like partice-in-cell, Monte Carlo (MC) [37–39], or solutions of the Boltzmann kinetic equation [2, 4, 32, 36, 40, 41], directly yield an electron velocity distribution function (EVDF) as a function of space, velocity, and time $f(\mathbf{r}, \mathbf{v}, t)$. If electron velocity space dynamics are of importance then a particle based method should be used, in lieu of a fluid model as demonstrated in previous studies [13].

In this study we have selected three approaches to fluid modeling, and examined the results and subsequent appropriateness of each model towards describing interfacial electron transport between gas and liquid densities of liquid argon. Here we present a brief overview of the selected fluid models, with the finer details of the origins and formulations of the models deferred to previous comprehensive studies on fluid modeling specifically [4, 13–15, 31, 32].

2.1.1. Drift diffusion models. The most popular approach to fluid modeling of electron transport in gaseous plasmas has traditionally been a hydrodynamic drift diffusion continuity equation (1) of the electron density, $n_e(z, t) = \int f(\mathbf{r}, \mathbf{v}, t)\mathrm{d}\mathbf{v}$. The electron flux is obtained by assuming a steady-state of the

momentum balance equation, and that the field-driven component of electron energy is much greater than the thermal contribution [15, 32, 36, 42]. The generalized one-dimensional continuity equation is

$$\frac{\partial n_e}{\partial t} - \frac{\partial}{\partial z}\left(n_e W + D\frac{\partial n_e}{\partial z}\right) = n_e(\nu_I - \nu_a - \nu_r), \quad (1)$$

where input data terms are the drift velocity, W, diffusion coefficient, D, and ionization/attachment/electron–ion recombination collision rates, ν_I, ν_a, and ν_r. All input data are assumed to be functions of the local instantaneous reduced electric field, $\frac{E}{n_0}$, where E is the instantaneous electric field and n_0 is the neutral atom density.

Interpolation of steady state transport coefficients and collision rates is used to provide values for these input parameters. The steady state values are obtained from the steady state EVDF which can be found via MC simulations [37, 43] or a multi-term kinetic solution of the Boltzmann equation [17, 30, 35, 44], given appropriate microscopic inputs of electron scattering cross sections for the target gas (see section 2.2).

In addition to the electron continuity equation (1), continuity equations for the creation of positive, n_+, (via ionization reactions) and negative, n_-, (via attachment reactions) ion densities are used

$$\frac{\partial n_+}{\partial t} = n_e(\nu_I - \nu_r), \text{ and } \frac{\partial n_-}{\partial t} = n_e\nu_a, \quad (2)$$

where ion transport has been neglected over the transient time scales considered in this study for ionization front propagation [4, 15] owing to the significantly reduced mobility and diffusion of molecular ions [45, 46].

Alongside the continuity equations for charged species densities (1), (2), the space charge effects on the electric field, E, must be computed to determine any screening effects due to the creation of electrons and ions. To accommodate a spatially varying dielectric permittivity in an inhomogeneous, isotropic material we self-consistently solve

$$\frac{\partial}{\partial z}(\varepsilon_r(z)\varepsilon_0 E) = e(n_e + n_- - n_+), \quad (3)$$

$$E = -\frac{\partial \varphi}{\partial z}, \quad (4)$$

where e is the elementary charge, $\varepsilon_r(z)$ and ε_0 are the fluid's relative and the vacuum dielectric permittivities respectively. Boundary conditions are supplied on the electric potential are $\varphi(0, t) = 0$ and $\varphi(L, t) = \varphi_{\text{applied}}$ where φ_{applied} is a fixed voltage to produce the desired applied electric field in the absence of space-charge contributions.

While the model described by (1)–(4) has been traditionally used to describe charged particle transport within gases, the functional form of the model has been demonstrated to be applicable to describe transport within liquid discharges assuming appropriate modifications to the input data are made [13]. As the neutral density increases the single-scattering assumption used for gas transport breaks down as the effects of elastic coherent scattering and electron interaction potential screening and polarization become important [17, 29, 30]. These effects are significant when the electron de Broglie wavelength is comparable to the average background particle spacing, $\lambda \sim n_0^{-\frac{1}{3}}$, which corresponds to low-energy electron scattering or scattering in very dense liquids.

Comprehensive formulations are available on how to modify gas phase electron interaction cross sections of non-polar atomic targets, such as noble liquids, to account for coherent scattering [30], and later the interaction potential screening and polarization [16, 29]. These structure modifications were implemented through a density dependent momentum transfer cross section (MTCS)

$$\Sigma_m(\nu, n_0) = 2\pi \int_0^\pi \Sigma(\nu, \chi, n_0)[1 - \cos\chi]\sin\chi \mathrm{d}\chi, \quad (5)$$

where ν is the incoming electron speed, χ is the electron scattering angle off the target atom, and $\Sigma(\nu, \chi, n_0)$ is an effective differential cross section including coherent scattering and interaction potential modifications via

$$\Sigma(\nu, \chi, n_0) = \tilde{\sigma}(\nu, \chi)S(\Delta k; n_0), \quad (6)$$

where $\tilde{\sigma}(\nu, \chi)$ is the liquid phase differential cross section containing any screening and polarization effects [16, 29], $S(\Delta k; n_0)$ is the static structure factor and $\Delta k = \frac{2m_e\nu}{\hbar}\sin\frac{\chi}{2}$ is the wave number proportional to the change in momentum [30], where m_e is the electron mass and $\hbar$ is reduced Planck's constant. The static structure factor is a nonlinear function of n_0 of the target material, and may be calculated from molecular simulations, measured via experiments [29, 30, 37], or derived analytically through solutions of pair-correlation functions as per the Verlet–Weis corrected Percus–Yevick structure factor [47]. For detailed discussion on the static structure factor, and its implementation in liquid scattering, readers are directed to previous studies [29, 30, 37].

These fundamental liquid transport studies demonstrated substantially different cross sections for liquid transport at low incoming electron energies compared to transport in gas phase, particularly in reduced momentum transfer from preferential forward scattering [16, 29]. It was shown that, while energy transfer was impacted by modifications of the cross section due to potential screening, energy transfer was not explicitly modified by including coherent elastic scattering effects [30, 31] and energy transfer due to inelastic excitation collisions is considered localized to the immediate target atom. In summary, the functional form of the balance equations used to model electron transport is the same whether transport is in gas or liquid. However, explicit modifications to include liquid phase physics must be performed [17, 30] to obtain the appropriate cross sections for computing electron transport data. If the correct cross sections are used to generate input data for either gas or liquid transport, then the drift diffusion model (1), (2) can then be applied directly.

2.1.2. Higher order models. In addition to drift diffusion fluid models, so called higher order fluid models have gained

popularity for modeling charged particle transport in plasmas [4, 13, 35, 48]. In these models, the hierarchy of velocity moments of Boltzmann's equation is not truncated at the electron flux, but often extends to include four continuity equations for electron density, n_e, electron particle flux, $\Gamma = n_e\langle \mathbf{v}\rangle = \int f(\mathbf{r}, \mathbf{v}, t)\mathbf{v}\mathrm{d}\mathbf{v}$, electron mean energy density, $n_\epsilon = n_e\langle\epsilon\rangle = \int f(\mathbf{r}, \mathbf{v}, t)\frac{1}{2}mv^2\mathrm{d}\mathbf{v}$, and electron energy flux, $\Gamma_\epsilon = n_e\langle\boldsymbol{\xi}\rangle = \int f(\mathbf{r}, \mathbf{v}, t)\frac{1}{2}mv^2\mathbf{v}\mathrm{d}\mathbf{v}$, where $\langle\mathbf{v}\rangle$, $\langle\epsilon\rangle$, and $\langle\boldsymbol{\xi}\rangle$ denote the electron average velocity, average energy, and average energy flux. Following the formulation of a four moment higher order model benchmarked in gas and liquid transport [13], we employ the following generalized model equations, in addition to the ion continuity equations (2)

$$\frac{\partial n_e}{\partial t} + \frac{\partial \Gamma}{\partial z} = n_e(\nu_I(\langle\epsilon\rangle) - \nu_a(\langle\epsilon\rangle) - \nu_r(\langle\epsilon\rangle)), \tag{7}$$

$$\frac{\partial \Gamma}{\partial t} + \frac{\partial}{\partial z}(n_e\theta_m(\langle\epsilon\rangle)) + n_e\frac{e}{m_e}E = -\Gamma\nu_m(\langle\epsilon\rangle), \tag{8}$$

$$\frac{\partial n_\epsilon}{\partial t} + \frac{\partial \Gamma_\epsilon}{\partial z} + eE\Gamma = -nS_\epsilon(\langle\epsilon\rangle), \tag{9}$$

$$\frac{\partial \Gamma_\epsilon}{\partial t} + \frac{\partial}{\partial z}(n\theta_\xi(\langle\epsilon\rangle)) + n\theta_m(\langle\epsilon\rangle)eE + n_\epsilon\frac{e}{m_e}E = -\Gamma_\epsilon\nu_\xi(\langle\epsilon\rangle), \tag{10}$$

where input data is required via collision rates for ionization, ν_I, attachment, ν_a, electron–ion recombination, ν_r, momentum transfer, ν_m, energy transfer, S_ϵ, energy flux transfer, ν_ξ, and higher order tensor product closure approximations, θ_m, and θ_ξ.

In this model, the higher order moments, $\theta_m = \langle v_z v_z\rangle$ and $\theta_\xi = \left\langle\frac{1}{2}mv^2v_zv_z\right\rangle$, are closed by evaluation over the equilibrium steady-state EVDF used to also evaluate collision input rates, similar to that of the input data described in section 2.1.1. While we choose to specify generic expectation value expressions for θ_m and θ_ξ, to facilitate computation via any particle based method, we note that under the formalism of a three-term decomposition of the EVDF these expressions yield the exact results presented by Becker and Loffhagen [35]. The virtues of this closure technique were demonstrated previously [13] to provide a parameter free, physically sound alternative to other closure assumptions, such as non-physical heat flux assumptions or parameterization in terms of $\langle\epsilon\rangle$, previously used in literature [4, 13, 48].

The same process for generating a look-up table of steady state input data via an equilibrium EVDF, described in section 2.1.1, is used for this higher order model also. Higher order models differ to drift-diffusion models because more information of electron dynamics is natively included, so that phenomena such as temporal and spatial non-locality can be resolved [15]. In lieu of using $\frac{E}{n_0}$ to determine input data as per the drift-diffusion model, here the electron mean energy, $\langle\epsilon\rangle$, is used as the interpolating variable to determine input data at each point in space during the simulation [49].

As discussed in section 2.1.1, for a local field dependent model, a higher order model can also be equally applicable in gas or liquid, assuming the correct modifications have been made to generate accurate input data to account for liquid effects. For further details on the higher order moment model used in this study we refer the reader to a recent formulation and benchmarking study [13].

2.2. Transport data in gaseous and liquid argon

Following the generalized fluid models presented in the previous section, we present the electron scattering cross sections for gaseous and liquid argon, in addition to the resulting argon transport and collision data that serves as input to the fluid models presented in section 2.1. It should be noted that this study assumes that ion transport is neglected over the timescales studied [45, 46], and that, for simplicity, singly ionized molecular argon ions are only considered in this study. Furthermore, electron–ion recombination and the formation of excited states are neglected in this study as it was found that at the applied reduced fields used in this study, for the electron and ion densities in liquid argon, the resulting recombination rates [50–54] were significant orders of magnitude less than the other collisional processes considered in this work.

2.2.1. Electron scattering cross sections. As this study involves both gas and liquid extremes of argon we require two sets of electron scattering cross sections in order to generate input data for fluid models. The gaseous argon electron scattering cross sections of Hayashi [55, 56] were used as input to a multi-term solution of the Boltzmann equation [16, 17, 31] to generate input data for this study. The set comprising of an elastic MTCS, twenty five inelastic excitation cross sections, and an ionization cross section were retrieved from the online database www.lxcat.net.

As recommended by recent studies of electron transport and negative planar streamer fronts in atomic liquids [57, 58], liquid argon cross sections were compiled from recent works on accurate low-energy liquid cross sections, combined with necessary modification of the gas phase Hayashi cross sections for inelastic processes. To form the basis of the MTCS scattering cross section, the low-energy ($\leqslant$10 eV) MTCS for liquid argon proposed by Boyle *et al* [16] was taken in order to include the effects of coherent scattering and atomic potential screening which are critical for low-energy electron scattering in dense liquids. At higher incoming electron energies, where the liquid cross section converges to the gas cross section, the gaseous argon MTCS of Hayashi [55] was once again used. These two elastic scattering cross sections were joined and smoothed at $\sim$10 eV to form a single elastic scattering cross section.

As precise measurements, or calculations, of liquid phase ionization cross sections do not exist for atomic argon, a liquid argon ionization cross section was constructed by modifying the gaseous argon ionization cross section as detailed in [59–62]. The liquid argon ionization threshold energy, I_{liq}, was computed by modifying the gaseous argon threshold energy, $I_{\mathrm{gas}} = 15.68$ eV, to account for dense liquid effects. The known gaseous ionization cross section of

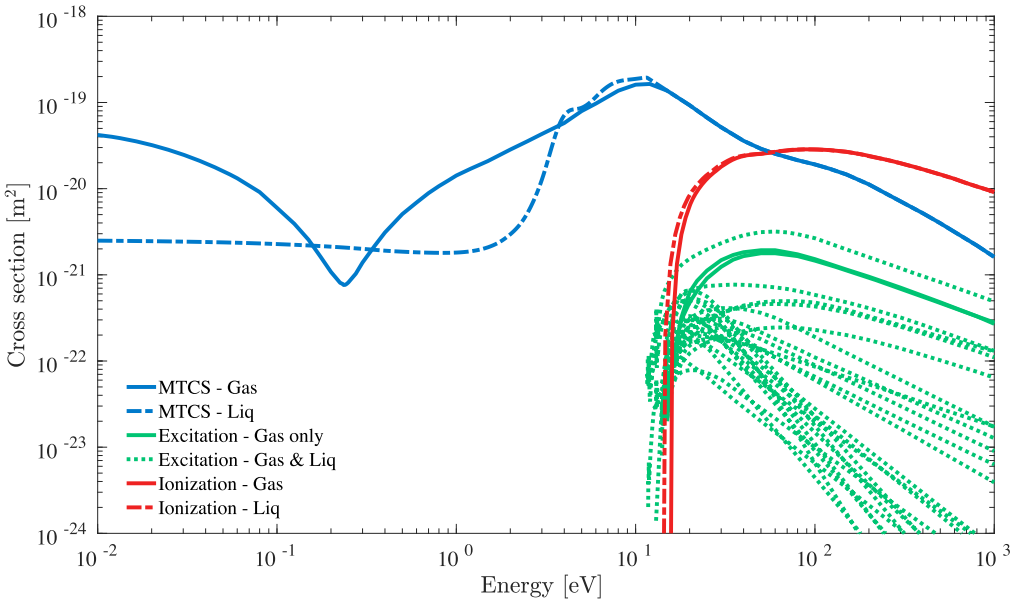

Figure 1. Gas and liquid argon electron scattering cross sections utilized in this study. Gas cross section data of Hayashi [55] via www.lxcat.net. Liquid cross section data of Boyle *et al* [16] and necessary modifications of Hayashi set detailed in section 2.2.1.

Hayashi [55] was then translated to the new threshold energy for liquid. The foundation and derivation of these modifications are detailed in [59], and the key result relevant to this present study can be summarized by the expression

$$I_{\text{liq}} = I_{\text{gas}} + P_{+} + V_0 + E_{\text{val}}, \tag{11}$$

where P_{+} is the ion polarization energy of the positive ion ($P_{+} = -1.08$ eV for argon [59]), V_0 is the energy of the delocalized electron level in the liquid i.e. the bottom of conduction band ($V_0 = -0.3$ eV for the liquid argon density used in this study [60]), and E_{val} is the change in energy of valence bands due to condensing the gas ($E_{\text{val}} = 0.1$ eV for argon [59]). This process yields the ionization threshold energy of $I_{\text{liq}} = 14.4$ eV.

In order to account for excitations in the liquid state, the set of inelastic atomic excitation cross sections of the Hayashi database was slightly modified to form a set of excitation cross sections for intermediate excitons in liquid argon [57, 58]. This is informed by the work of Laporte *et al* [63], which demonstrated that as dilute rare gases are compressed to high, liquid densities the presence of atomic excitations is replaced by excitations of intermediate excitons in the liquid phase [63]. As these intermediate excitons have a unique parentage, via the isolated atom's excited states [64, 65], we thus approximate the cross sections for intermediate exciton excitations by cross sections of the corresponding atomic excitations.

The threshold energies of the adopted excitation cross sections are unmodified from the atomic excitations out of necessity, because complete threshold energies for excitons in liquid argon are not available in the literature, especially for the optically forbidden transitions. This assumption is supported by the fact that thresholds for known intermediate excitons in liquid rare gases (argon, krypton and xenon) are very close (within 5%) to the thresholds of atomic excitations [63, 65].

Finally, the reflectivity spectra of solid argon reported by Haensel *et al* [66] demonstrated that lines below 14.5 eV correspond to discrete excitonic states, while lines above 14.5 eV correspond to continuous interband transitions. We have therefore excluded the two atomic excitations which have thresholds above 14.5 eV (being 14.71 and 15.2 eV) as their energies are in the region of continuous band to band transitions. The final sets of electron scattering cross sections in both gaseous and liquid argon are shown in figure 1.

2.2.2. Fluid model input electron transport data. Using the electron scattering cross sections for both gas and liquid argon extremes (see figure 1) equilibrium electron transport data was calculated to serve as input data for the fluid models used in this study. A multi-term solution of the Boltzmann kinetic equation [16, 17, 31] was used to calculate EVDFs over a range of reduced electric field values at 85 K, a common cryogenic temperature, near the triple point, used in argon applications and experimental studies [51, 67–69]. These velocity distribution functions were then used to calculate the flux transport coefficients necessary for input to the drift-diffusion fluid model (1). Plots of electron drift velocity, longitudinal diffusion, and ionization collision rate, used as input for (1), (2), are shown in figure 2; though not used as a model input, a plot of the electron mean energy as a function of reduced field is included to demonstrate key differences between gas and liquid transport.

Reduced collision rates for input to the higher order fluid model are directly computed from spatially homogeneous steady-state EVDFs found via multi-term solution of the Boltzmann equation [17], these rates are presented in figure 3 demonstrating the variation of collision rates for momentum

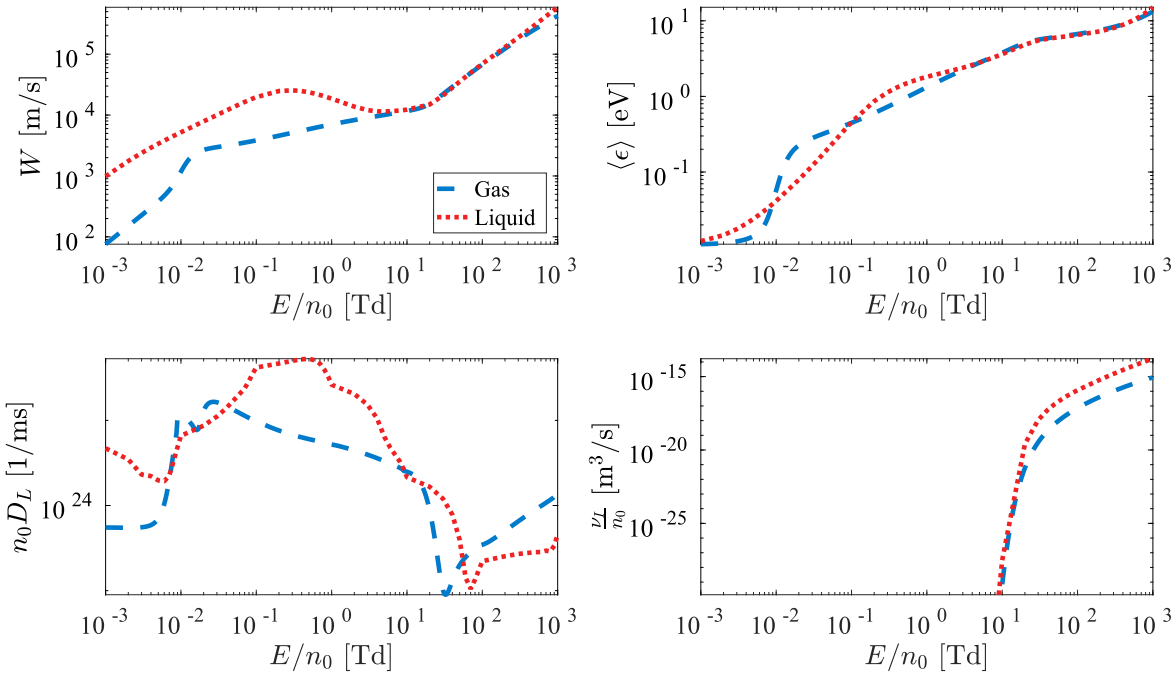

Figure 2. Input transport data of electrons in argon for local-field dependent electron fluid models. Dashed lines denote gas transport, dotted lines denote liquid transport. (Top-left) Drift velocity versus reduced field. (Top-right) Electron mean energy versus reduced field. (Bottom-left) Longitudinal reduced diffusion coefficient versus reduced field. (Bottom-right) Reduced ionization collision rate versus reduced field.

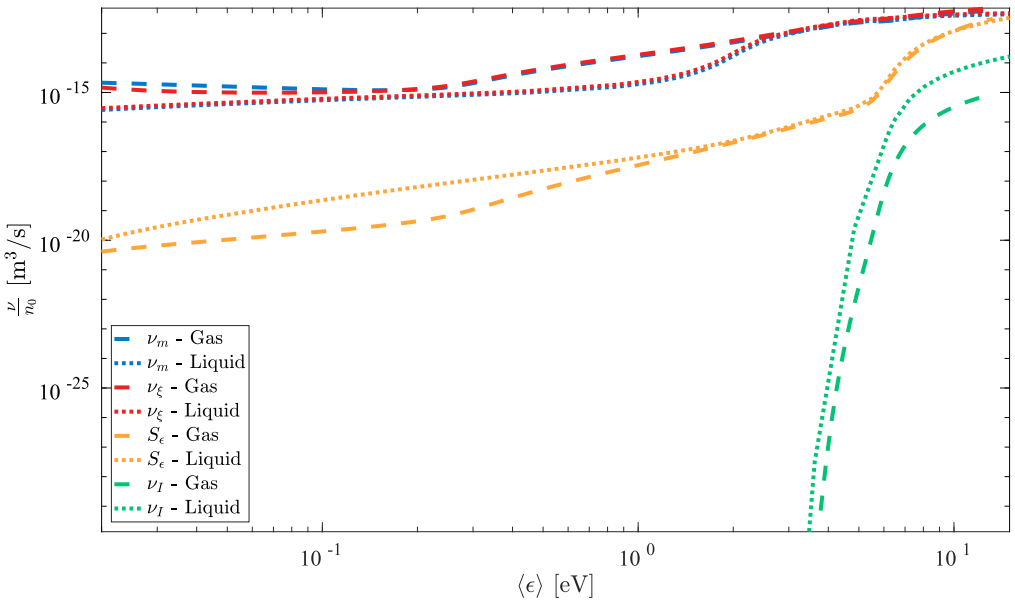

Figure 3. Input collision rates of electrons in argon for mean energy dependent higher order fluid model. Dashed lines denote gas transport, dotted lines denote liquid transport.

transfer ν_m/n_0, energy flux transfer ν_ξ/n_0, lumped energy loss S_ϵ/n_0, and ionization ν_I/n_0.

3. Modeling at the gas–liquid interface

Following the brief review of fluid modeling methods and associated input data for electrons in either gas or liquid presented in section 2, we now discuss necessary interfacial effects that should be considered when trying to model electron transport between gas and liquid extrema as a continuous process. We consider four important factors of the gas–liquid interface model: (i) functional form of the variation in n_0, (ii) variation of input data for fluid models across the interface, (iii) variation of the delocalized electron energy level, V_0, across the interface, and (iv) variation of the relative dielectric permittivity, ε_r, across the interface. In this study we examine the effects of differing treatments of (i) the form of the interface, as well as (ii) the type of input data used in the models. The presence of spatially varying (iii) delocalized

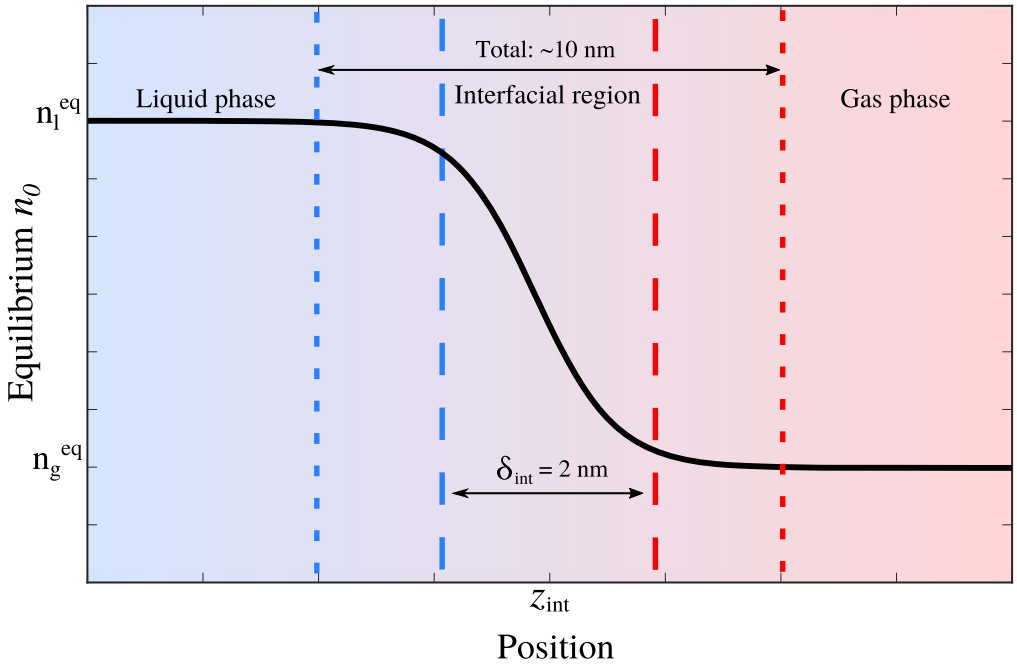

Figure 4. Equilibrium argon vapor–liquid interface as determined by molecular dynamics simulations [70, 71, 73]. The approximate length of the full interface transition region as well as the 90%–10% parameter length, δ_{int}, used in this study are marked explicitly.

electron energy level, V_0, and (iv) relative dielectric permittivity, ε_r, are assumed fixed properties in this study as they present essential physics, induced by large atomic densities, that cannot be ignored when simulating the gas–liquid interface.

3.1. Density profile variations

In order to accurately model electron transport between a gas phase plasma and a condensed liquid, the structure of the interfacial region must be known. For this study, we assume the existence of an equilibrium interfacial density profile formed between gas and liquid phases for atomic fluids, as outlined in figure 4. The existence of this interfacial profile in non-polar atoms, such as argon and xenon, has been probed in various molecular dynamics and MC studies [70–73]. These simulations employ Lennard-Jones (LJ) potentials as an approximation to the atomic interaction potentials between each atom of noble liquid [70–73]. Key measurables from these studies were equilibrium liquid and vapor densities, surface tension, and interface layer thickness.

Of particular use in this study, is a commonly proposed functional form describing the interfacial atomic density variation via a hyperbolic tangent function [73, 74]

$$n_0(z) = \frac{1}{2}(n_g^{\text{eq}} + n_l^{\text{eq}}) - \frac{1}{2}(n_g^{\text{eq}} - n_l^{\text{eq}}) \tanh\left(\frac{2(z - z_{\text{int}})}{\delta_{\text{int}}}\right), \tag{12}$$

where n_g^{eq} and n_l^{eq} are the gas and liquid equilibrium densities, z_{int} is the center position of the interface, and δ_{int} is a measure of the thickness of the interface, defined as the distance between 90% and 10% of the liquid density. From previous studies conducted on the existence of noble liquid interfaces, the value of δ_{int} is around $5\sigma_{\text{LJ}}$, where $\sigma_{\text{LJ}} = 0.34$ nm is the atomic diameter [68, 70, 71, 73, 74], while the liquid–vapor density ratios (n_l^{eq}:n_g^{eq}) were found to vary from 200:1 up to 500:1, depending on the cut-off distance employed in the LJ potentials [71, 73, 74].

3.2. Fluid model input data for continuum models between gas and liquid phases

With a well defined density configuration of the equilibrium interface between gas and liquid argon extremes, we now consider the effects of this density variation on the required fluid model input data. One question that we wish to probe in this study, is whether or not we must use n_0 dependent input data between gas and liquid density extremes, or if we can simply use pure gas and liquid data either side of a defined interface point, z_0, akin to a step-function profile. One factor to consider in answering this question is the electron-neutral collisional mean free path

$$\lambda_{\text{mfp}} \approx \frac{1}{n_0 \sigma}, \tag{13}$$

where n_0 is some neutral background density and σ is an electron scattering cross section. For gas, liquid, or intermediate densities, a range of mean free paths can be calculated to determine if the collisional scattering dynamics and any non-equilibrium behavior will impact transport in the interfacial transition between gas and liquid. Typical liquid argon densities are $n_l^{\text{eq}} \approx 10^{28}\,\text{m}^{-3}$ while the gas density at the equilibrium interface used in this study is roughly 300 times smaller than the liquid, resulting in mean free paths for electron scattering in liquid argon in the range 1–100 nm, while the corresponding mean free path range in gaseous argon is 0.3–30 μm. Since the equilibrium interfacial region

in argon is on the order of nanometers we must consider n_0 dependence in fluid model transport data in this interfacial region.

We now appropriately label fluid models introduced in section 2.1, and define explicitly whether n_0 dependent input data is used. Firstly, the simplest fluid model used in this study is a local-field dependent drift-diffusion model (1), (2), utilized with n_0 dependent input data to allow for both gaseous and liquid background media. This dependence is introduced by asserting the W, D_L and ν_I input parameters of (1), (2) are now functions of both the instantaneous reduced electric field and neutral density across the interface, $f\left(\frac{E}{n_0}\right) \rightarrow f\left(\frac{E}{n_0}, n_0\right)$. This model will henceforth be referred to as the *LFA* model.

Finally, taking the higher order model presented in (7)–(10) we recast the functional form of the input parameters such that any input parameter dependent on electron mean energy is now also a function of the neutral density $f(\langle\epsilon\rangle) \rightarrow f(\langle\epsilon\rangle, n_0)$. As this is a higher order four moment model this model will henceforth be referred to as the *4MM* model. Input data requirements accounting for the density variation for both the LFA and 4MM models are discussed and presented in appendix A using the results of a recently proposed and benchmarked study [75].

3.3. Space-charge field and spatially varying permittivity

Self-consistent solution of the electric field was performed via solution of (3) and (4) where the functional form of the spatially varying relative dielectric constant, $\varepsilon_r = \varepsilon_r(z)$, was specified using the same tanh function (12) used to modulate n_0, where liquid and gaseous argon constants were taken as $\varepsilon_r^l = 1.504$ and $\varepsilon_r^g = 1.000\,5$ respectively [76].

3.4. Accommodating spatial variation of V_0 across the interface

As gas densities increase to liquid values, we need to also consider the variation in the energy of the delocalized electron level in the liquid, V_0. This can be positive (neon, helium) or negative (argon, xenon) and is largely a function of the electron scattering length of the target atom [59, 60]. The dependence of V_0 on the neutral atomic density of argon, n_0, demonstrates an approximate linear roll-off from 0eV in gas down to approximately -0.3 eV at the maximum liquid density used in this study [59, 60]. Given a known equilibrium $n_0(z)$ profile, and thus an equilibrium $V_0(z)$, an effective electric field is found by differentiating $V_0(z)$, and combined with the electric field, E, computed via (3) to yield the total electric field

$$E_{\text{total}} = E + E_{V_0}. \tag{14}$$

4. Results and discussion

Using the fluid models and input data presented in sections 2 and 3, we present results and discussion for two prototype interfacial problems. Section 4.2 presents transient simulations of an electron swarm propagating from liquid argon into gaseous argon (left to right in this study's frame of reference). Brief results of an ionization front in gaseous argon penetrating into liquid argon (from right to left) are presented in section 4.3. We believe it is most instructive to start investigations with essentially swarm transport in the liquid phase transitioning to gas phase, where fields and ionization rates are low, before considering cases where space-charge field considerations are important due to ionization events. To examine the impacts of electron transport experiencing a gas–liquid interface transition in cryogenic argon, we present results from (i) large macroscopic length scales to examine the overall qualitative nature of the results, and (ii) small length scales at the immediate vicinity of the interfacial region in order to examine the impact of the interface transition. Liquid to gas results of section 4.2 are presented at early (2 ps), intermediate (15 ps), and late (50 ps) times to demonstrate the physics of electron transport over different time scales, while the gas to liquid results of section 4.3 are taken at 50 ps. Finally, following the results of the two prototype problems (liquid to gas and gas to liquid), section 4.4 demonstrates the distinctly different results produced by electron transport simulations that assume a simple step function interface, in lieu of the equilibrium tanh function transition proposed in this work.

4.1. Simulation conditions

An applied reduced field magnitude of $|E/n_0| = 300$ Td in gas phase, corresponding to 0.8 Td in the liquid, was applied to drive electrons into the gas–liquid interface; the appropriate sign was assigned in each simulation to drive electrons left to right or vice versa. In this study the neutral atom temperature was kept constant at $T_0 = 85$ K, a commonly used cryogenic temperature for liquid argon experiments [21, 69, 77]. The neutral density, n_0, was varied using the tanh function interfacial density ramp (12), where $n_l^{\text{eq}} = 1.8 \times 10^{28}\,\text{m}^{-3}$ was obtained from the liquid argon coexistence curve at 85 K [77]. The van der Waals radius of argon $r_{\text{Ar}} = 188$ pm was used in computation of the Percus–Yevick structure factor [30, 37, 47]. Based on previous studies of equilibrium gas–liquid interface properties found in literature [70, 71, 73, 74], the ratio of equilibrium gas density to liquid density was assumed to be $n_g^{\text{eq}} = n_l^{\text{eq}}/300$, and the 10–90 interface width, δ_{int}, was assumed to be 2 nm. Using the specified reduced field strengths, and the density profile provided by a tanh function, the initial total effective reduced electric field (14) is shown in figure 5.

Naturally, the space-charge field effects will evolve over the course of simulations but by simply considering the initial total fields assists in understanding of the results presented in sections 4.2 and 4.3. From the liquid to gas plot of figure 5 it is clear that the effective field due to V_0 variation acts to impede electron transport from the liquid to the gas, while conversely it enhances electron transport into the liquid when the applied field is reversed on the right-hand plot.

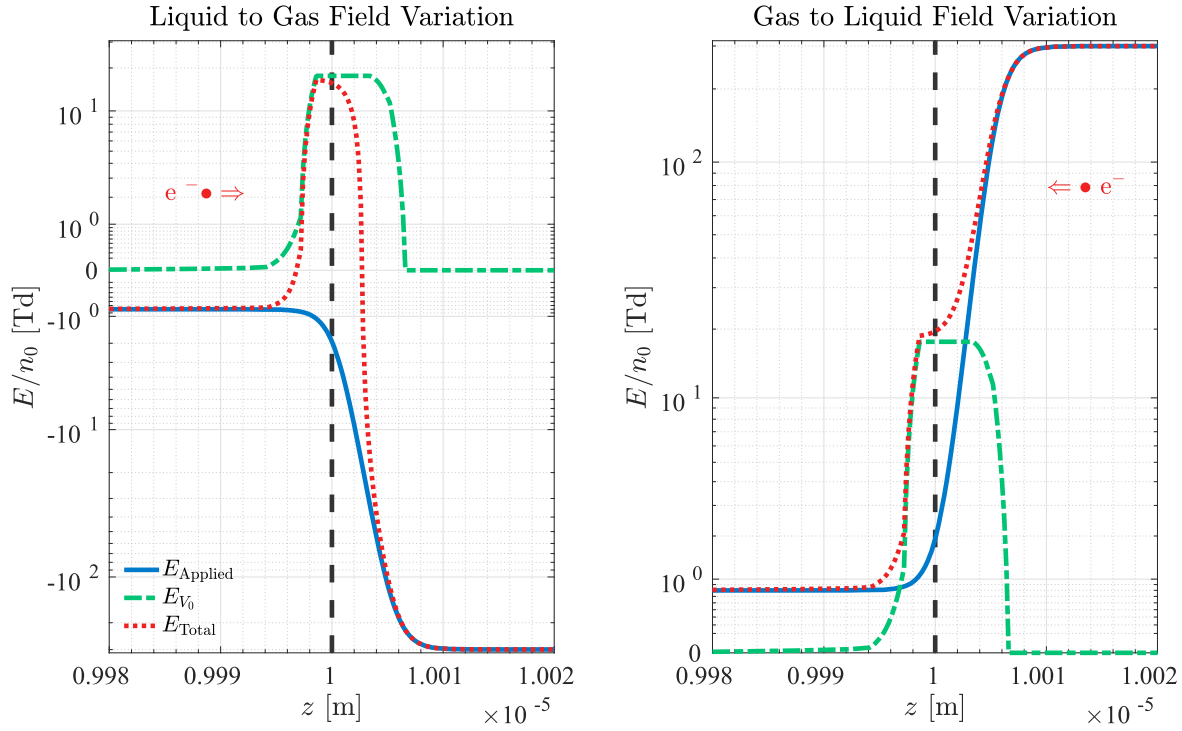

Figure 5. Reduced electric field profiles for applied and V_0 contributions for both simulation configurations presented. Note that symmetric logarithmic axes have been employed in this figure. The vertical dashed black line denotes the center point of the interface transition.

Initial conditions for simulation of streamer formation and propagation were assumed as a narrow Gaussian pulse of electron/ion densities created by an arbitrary ionization event prior to the simulation start. To ensure initial conditions did not experience immediate interfacial effects, initial charged particle densities for the liquid to gas simulation were set at 2 μm from the interface and the ionization front propagating from gas to liquid was set at 100 μm from the interface. Although there is no physical meaning to a mean energy in regions of zero density, the fluid model input parameters are interpolated from a mean energy value. Hence, to avoid numerical issues, we specify the initial values of mean energy, velocity and energy flux to be their steady-state values at the corresponding E/n_0 value, even in regions of zero density, as was done in previous fluid modeling studies [4, 13, 15]. At later times, when the density becomes non-zero, these fluid model parameters will then vary smoothly both spatially and temporally.

4.2. Electron transport from liquid argon into gaseous argon

Electron and ion density initial conditions of narrow Gaussian pulses were used in a simulation of electron transport across an interface, analogous to a single ionization event within a liquid argon detection chamber. Evolution of the electron density in figure 6 shows the initial pulse of electrons diffuses very quickly, leading to electron extraction from liquid into the gas phase as electrons impinge on the interface region. Qualitatively, both models predict similar results over all times however, it is clear the 4MM model demonstrates higher rates of electron extraction from the liquid. The LFA model predicts at least twice as much charge blocking on the liquid side of the interface compared to the 4MM model. Examining the expanded interfacial region of figure 6, we see the charge build-up at a narrow scale, with the 4MM result demonstrating two distinct roll-off gradients across the interface. To interpret this structure it is beneficial to consider the average electron velocity.

Figure 7 demonstrates that far from the interfacial region, the average electron velocity has relaxed to an equilibrium value. However, near the interface we see that initially the 4MM result predicts a large positive velocity, due to the large initial diffusive flux, and never becomes negative. In contrast, at the immediate vicinity of the interface the LFA model predicts a negative average velocity due to the blocking field contribution of the V_0 potential in liquid argon. As time continues, the magnitude of these initially large velocities decreases but their sign differences remain. As the distance over which the blocking field is applied is very small, and the time for mean energy relaxation is quite long, the mean energy does not rapidly respond to the field variation. This is an example of non-local electron transport that the LFA model cannot predict, but the 4MM model can. These major differences in the average electron velocity at the interface are the drivers for deviations in electron density results observed in figure 6.

The top half of figure 7 also demonstrates a short, but persistent, relaxation length on the liquid side of the interface well before the interface is encountered. We believe this gradual decrease in electron average velocity prior to the interface is a further demonstration of spatial non-locality being predicted by the mean energy dependent model, which the LFA model simply cannot predict owing to its reliance on

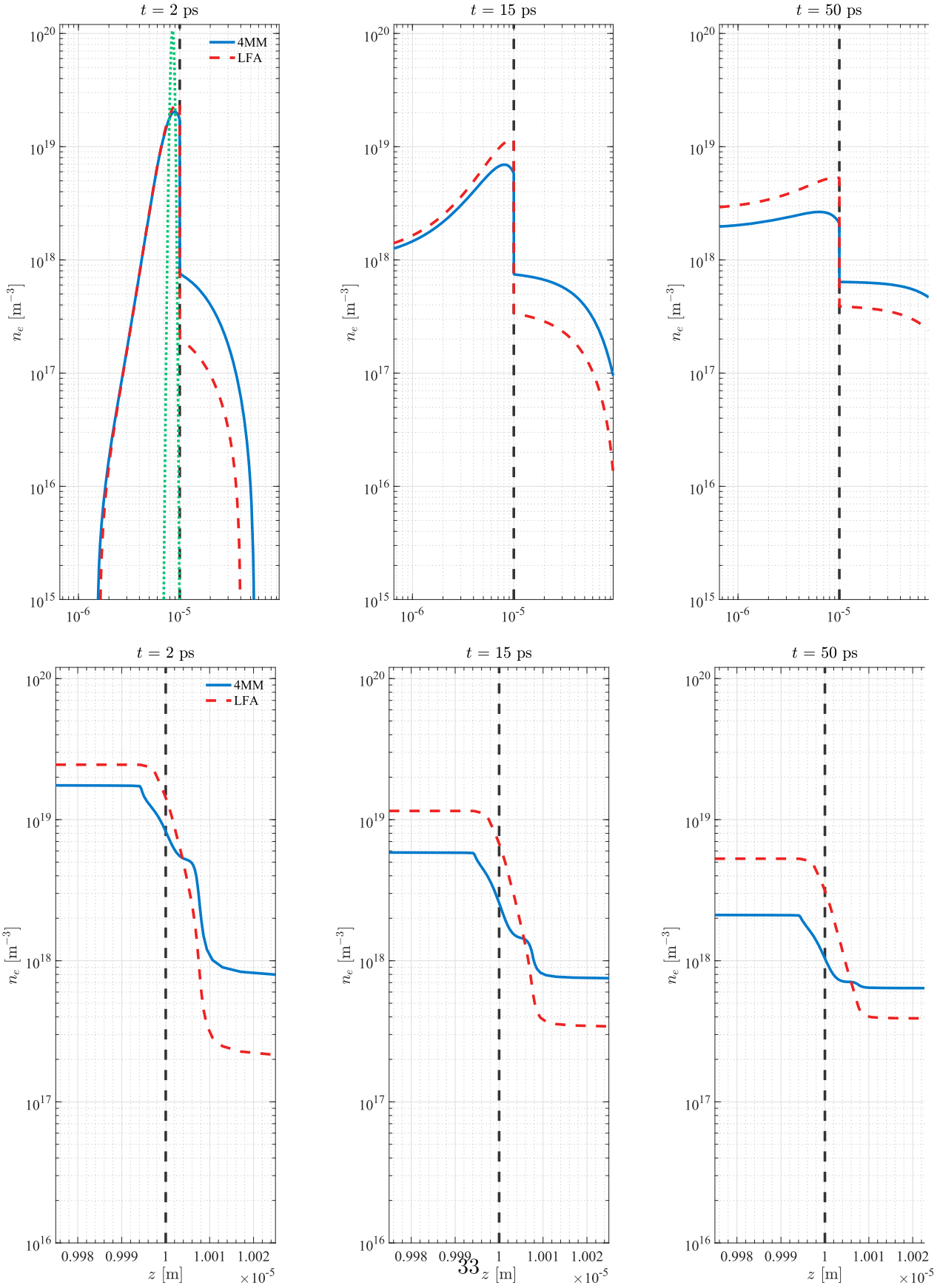

Figure 6. Electron density evolution for 4MM and LFA models at short, intermediate, and longer times as the electron swarm propagates from liquid to gaseous argon. Top view: macroscopic results. Bottom view: expanded view of interfacial results. Initial condition given by green dash–dot green line. Direction of field-driven propagation is from left to right.

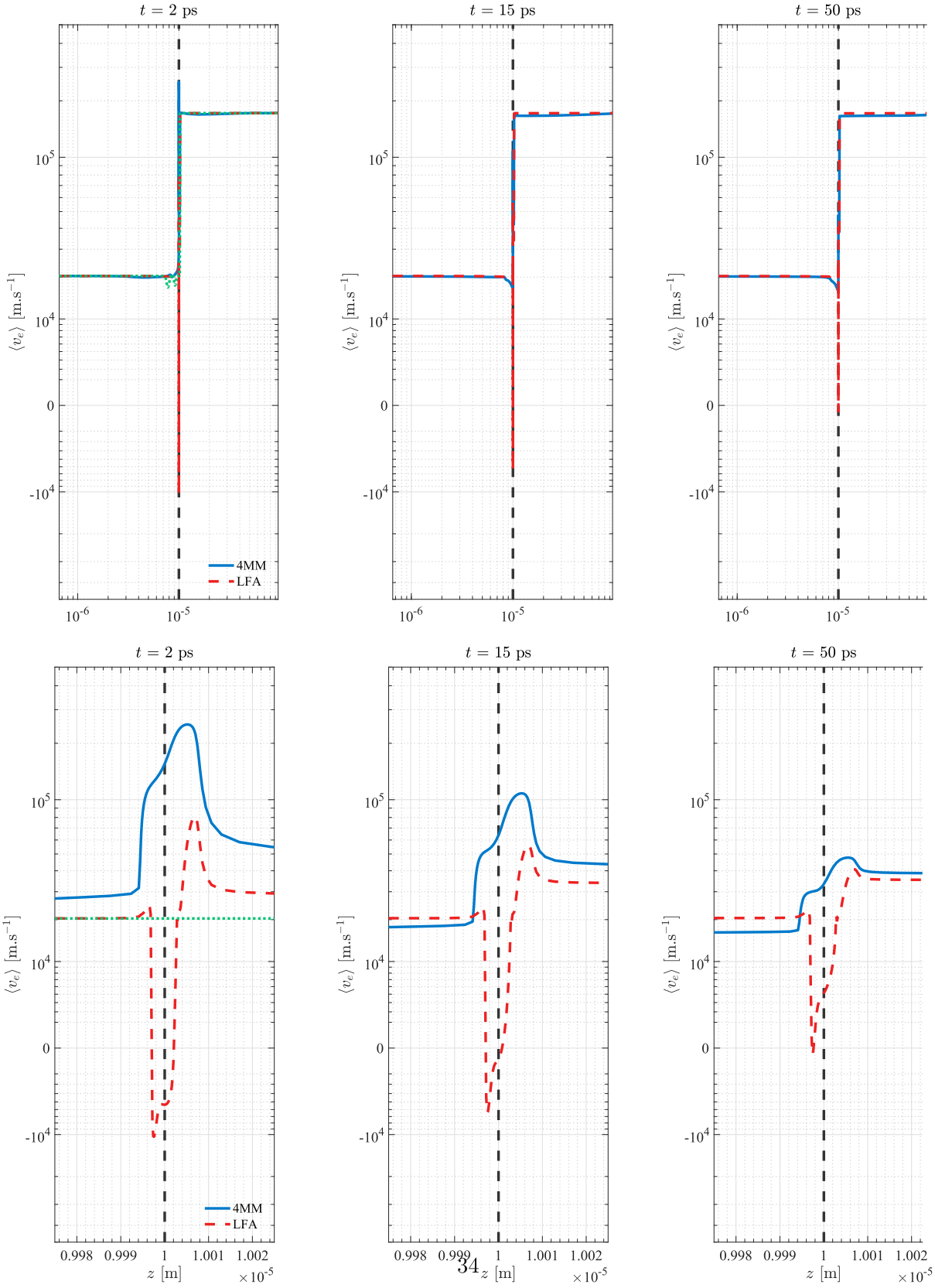

Figure 7. Average electron velocity for 4MM and LFA models at short, intermediate, and longer times as the electron swarm propagates from liquid to gaseous argon. Top view: macroscopic results. Bottom view: expanded view of interfacial results. Initial condition given by green dash–dot green line. Direction of field-driven propagation is from left to right. Note that symmetric logarithmic axes have been employed in this figure.

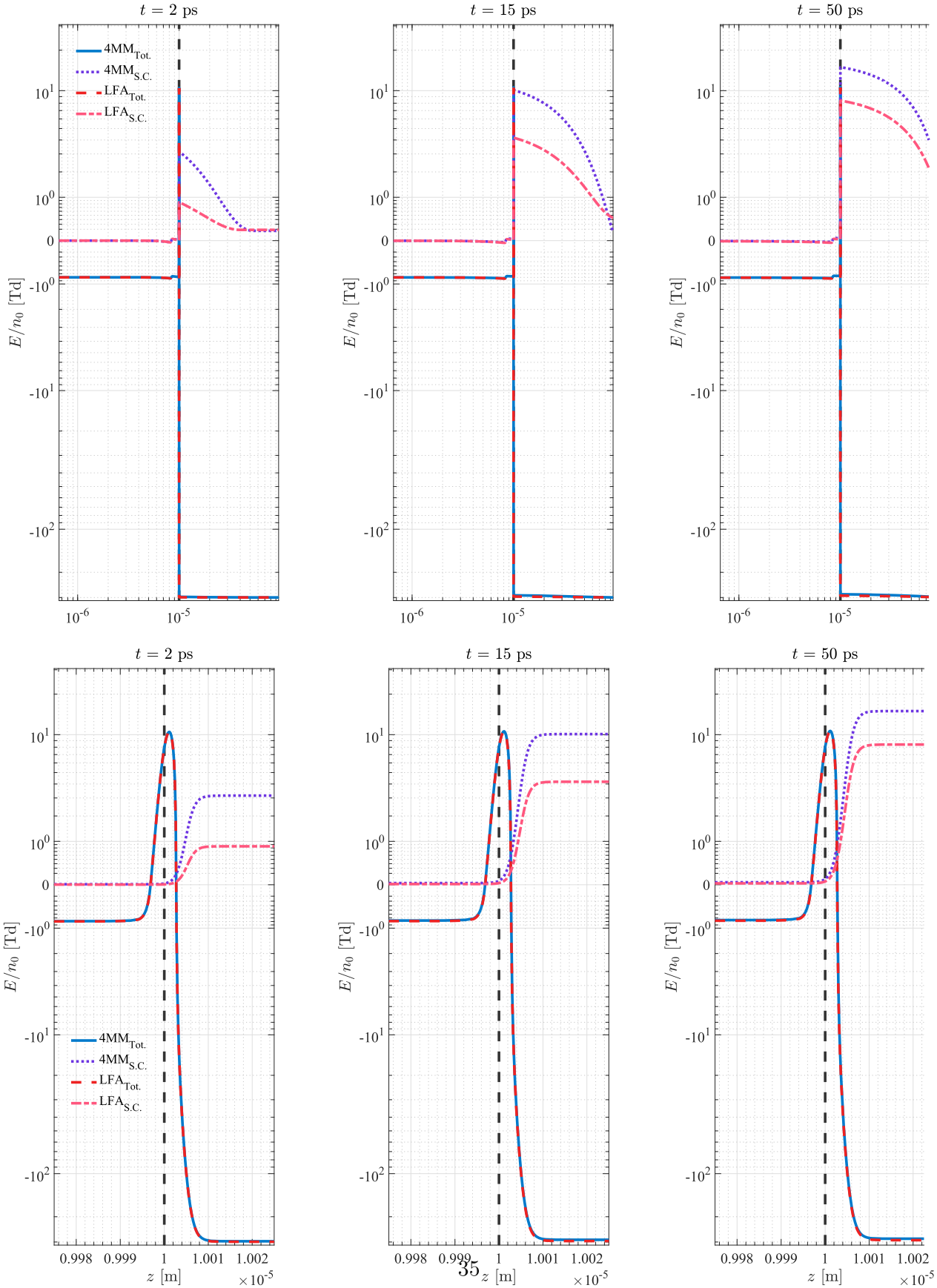

Figure 8. Total E/n_0 and space-charge contribution to E/n_0 for 4MM and LFA models at short, intermediate, and longer times as the electron swarm propagates from liquid to gaseous argon. Top view: macroscopic results. Bottom view: expanded view of interfacial results. Note that symmetric logarithmic axes have been employed in this figure.

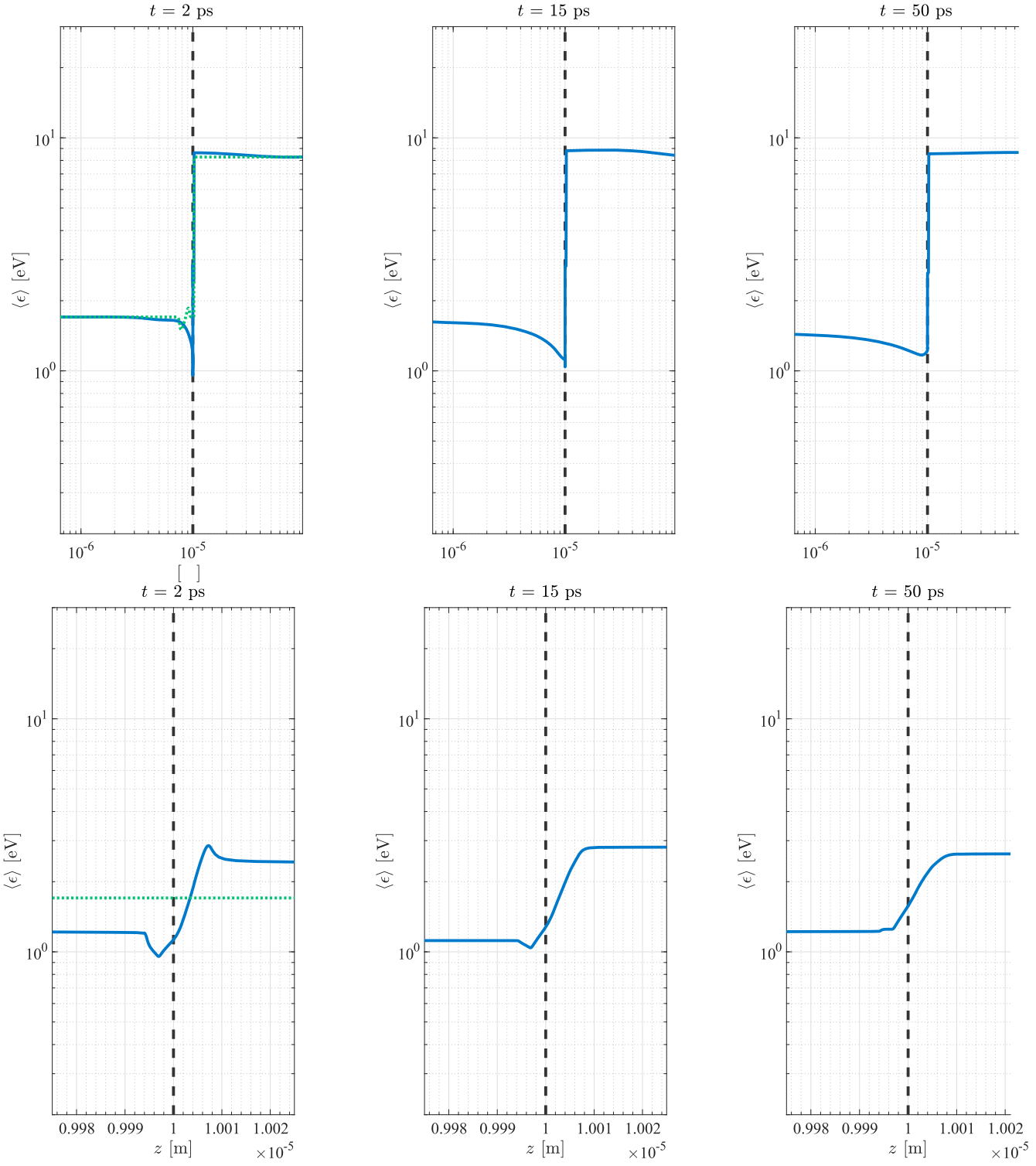

Figure 9. Electron mean energy for 4 MM model at short, intermediate, and longer times as the electron swarm propagates from liquid to gaseous argon. Top view: macroscopic results. Bottom view: expanded view of interfacial results. Initial condition given by green dash–dot green line. Direction of field-driven propagation is from left to right.

the instantaneous electric field, shown in figure 8. From figure 8 we cannot see a significant variation in the total E/n_0 over the lifetime of this transient simulation; this is a result of the space charge effects being small compared to the applied field, as indicated in the figure where we have plotted the isolated contributions of space-charge effects.

Figure 9 demonstrates the electron mean energy of the 4MM model to assist in interpreting the results of the preceding figures. We can clearly see a gradual relaxation of $\langle\epsilon\rangle$ on the liquid side of the interface, consistent with the observed non-local effects on electron transport in figure 7. Far from the interface the mean energy relaxes to the

equilibrium value given by the value of E/n_0 in the gas or liquid. We note a clear minimum in mean energy is observed at short times in the expanded interface region of figure 9 due to the relatively high transient electron flux, combining with the sign change of the blocking electric field provided by the V_0 potential, as a result of the $\Gamma \cdot E$ term in the energy balance equation (9). This energy reduction immediately at the interface is only present at short times because of the large initial diffusive electron flux. As this large initial diffusive flux subsides over time, the energy loss via the $\Gamma \cdot E$ term becomes less significant, demonstrated at 15 and 50 ps.

4.3. Electron ionization front transport from gaseous argon into liquid argon

We now briefly present and discuss results of directing an electron streamer front in gaseous argon into liquid argon. This simulation was performed under the same conditions as the previous section, apart from simply reversing the sign of the applied electric field to yield a total reduced electric field configuration as shown in figure 5. The initial condition to this simulation was provided by allowing a streamer front to form in gaseous argon, before imposing a gas–liquid interface transition approximately 100 μm in front of the streamer front.

For brevity, we present electron transport profiles after 50 ps, instead of multiple time points, in figure 10. Examining the LFA and 4MM results produced by the tanh interface assumption, we see that the initial electron density of the streamer tip is transported across the interface with a notable attenuation of the electron density further into the liquid. Examining the expanded view of the interface, the LFA model predicts a larger charge-build up at the gas side of the interface compared to the 4MM model consistent with a noticeably lower speed immediately at the interface, arising from the combination of the increase in n_0 at the interface as well as space-charge screening effects on E/n_0.

When comparing the average electron velocity plot, the most distinguished point of difference between the two models is the clear spatial relaxation length of $\langle v_e \rangle$ following the interface transition. Results of the 4MM model indicate a decay to the equilibrium drift velocity value observed in liquid argon, which demonstrates the presence of spatial non-locality which is not replicated by the LFA model. Additionally, a discrepancy arises between the two models at the expanded interface scale, where a smaller average velocity is produced by the LFA model as a result of a weaker reduced field occurring at the gas–liquid interface. In this range, the mean energy dependent 4MM model does experience a reduction in average velocity, but to a lesser extent than that found in the LFA results.

Finally, to assist further in interpreting the 4MM results, the electron mean energy is presented in figure 10. Here we note that in the expanded interfacial region of figure 10 a reduction in mean energy occurs on the gas side, due to increasing collisional energy losses from an increasing n_0, however the electron mean energy experiences a slight increase over the interface due to the restorative effects of the V_0 field via the $\Gamma \cdot E$ term in the energy balance equation (9). Once the effects of the interface transition have subsided, the mean energy decays to the equilibrium mean energy value for electrons in liquid argon with a clear relaxation length, indicating the presence of non-local electron transport.

4.4. Impact of step function input data

To determine if using a tanh function to modulate n_0 at the interface, which necessarily requires the density dependent fluid model input data, between gas and liquid extrema is actually required compared to simply using a standard step function variation in the density, we repeated the simulation of an ionization front propagating from gas to liquid. In this case we employed a step function transition between liquid on the left and gas on the right. For brevity, we present results at 50 ps in figure 10, demonstrating the vastly different qualitative results produced by assuming a step function transition.

From figure 10, we see that by assuming a step-function with the LFA model the electron densities are much higher over the macroscopic length scale. Approximately twice as many electrons are transported into the liquid as compared with any of the previous results. At the narrow length scale of the interface, we see the step-function LFA result actually decreases prior to the interface before experiencing a sharp build up of electrons on the liquid side; this is a starkly different qualitatively result compared to any of the previous results obtained using the smooth tanh function. On the other hand, while the step-function 4MM results are not equal to those achieved through the tanh assumption, they are very similar and produce no major deviations compared to the LFA results.

The step-function LFA electron density differences are consistent with a very high average velocity at the interface, demonstrated in figure 10, compared to any of the previous simulation results. This order of magnitude difference in the average velocity transports electrons into the liquid at a considerably higher rate compared to the results using the tanh interface assumption. This high average velocity occurs due to a large E/n_0, produced due to the small, gaseous argon value of n_0 assumed near the interface instead of a gradually increasing value. Once again, compared to the distinctly different observations of the LFA models we see no major deviation between 4MM results, with the only noticeable difference being the discontinuity immediately at the interface.

For completeness, figure 10 also shows the electron mean energy for the 4MM models using both tanh and step-function assumptions. We see no major differences in $\langle \epsilon \rangle$ for the two results, indicating why differences between 4MM results for the other variables were minimal. Since $\langle \epsilon \rangle$ is observably insensitive to the form of interface assumptions, and demonstrably a continuous variable, we believe that it is a much more reliable variable to use when determining input data compared to E/n_0 which suffers from being explicitly related to the assumptions we impose on n_0.

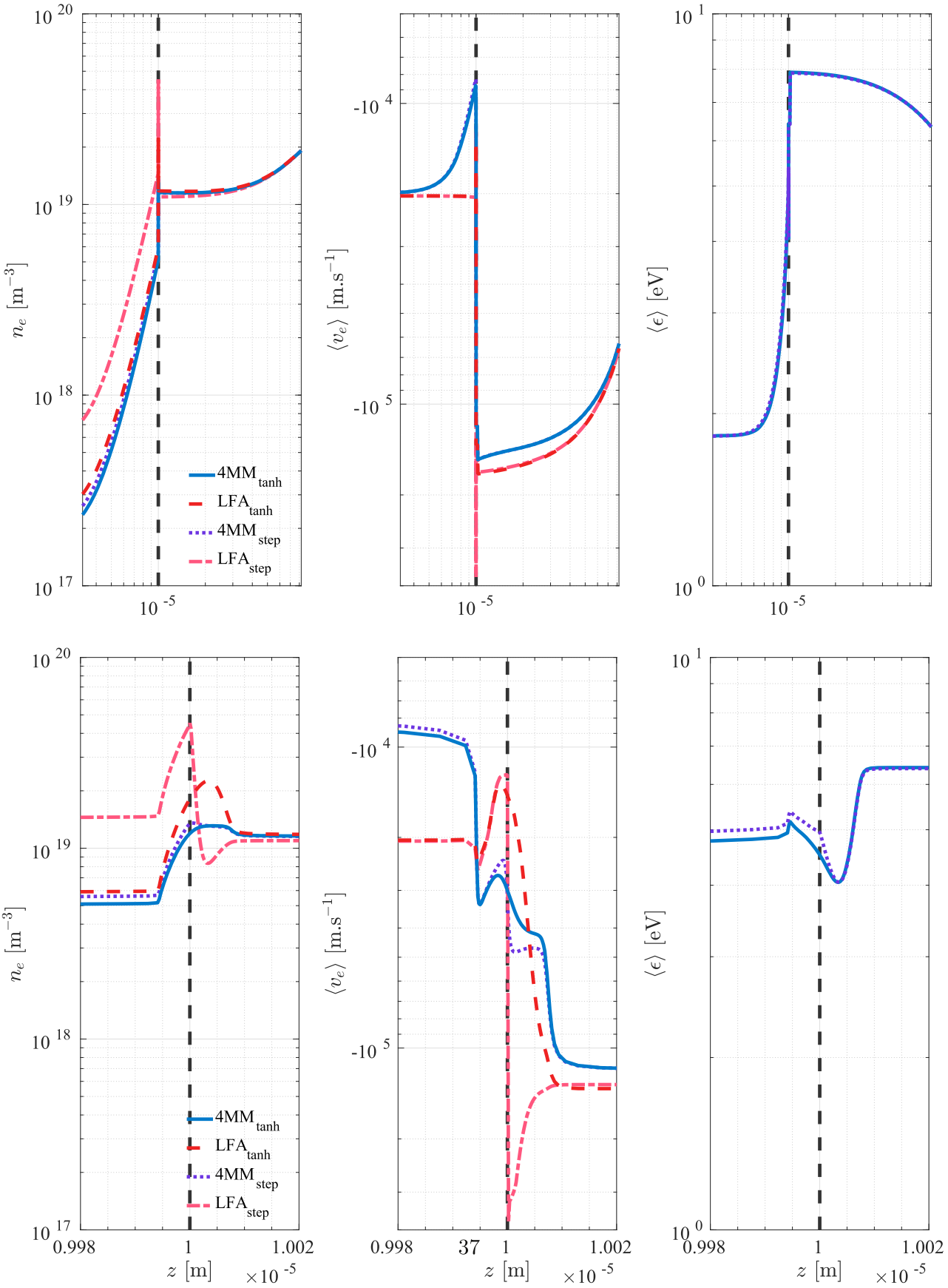

Figure 10. Electron density, average velocity and mean energy for 4 MM and LFA models after 50 ps of an electron streamer penetrating from gaseous to liquid argon. Results of assuming a tanh or step function interface on are shown for comparison. Top view: macroscopic results. Bottom view: expanded view of interfacial results. Direction of field-driven propagation is from right to left.

5. Conclusions

In this study we have presented results from multiple fluid models simulating (i) an electron swarm propagating from liquid argon into gaseous argon over an equilibrium interface density variation, and (ii) an electron streamer front being driven out of gaseous argon across the interface into liquid argon. We presented a method to account for large density variation from gas to liquid phase by assuming both a realistic density profile and step-function variation of n_0 in order to implement approximation rules for density dependent input transport data between gas and liquid extremes. Furthermore, we have accommodated interfacial effects of the spatial variation of both the dielectric constant, ε_r, through solution of Poisson's equation, and binding energy of an electron in liquid, V_0, through an effective applied electric field.

Using the proposed methods to compare local (LFA) and non-local transport (4MM) models and their sensitivities, our key recommendation to best describe electron transport between gas and liquid densities is to adopt a mean energy dependent higher order fluid model, such as the 4MM method used in this study. This model demonstrated greater flexibility and reliability in resolving non-local physics and interfacial electron transport compared to the local field drift-diffusion model. It was demonstrated that a drift-diffusion continuity equation (LFA) model required careful treatment of input data between gas and liquid extremes by way of approximating field dependent input data for intermediate densities using a tanh function, whereas the non-local 4MM model was relatively insensitive to the functional form of n_0 variation.

In summary, this work has presented the findings of a fundamental comparative modeling study of electron transport across cryogenic argon gas–liquid interfaces. We successfully demonstrated the importance of modifying gaseous electron transport models to account for interfacial and liquid effects when considering transport at the gas–liquid interface. A key message of this study is that vastly different electron transport is produced if gas phase input data is simply scaled to liquid densities, compared to using accurate liquid phase data. While this study has focused on a simple atomic liquid-gas system, we hope that this work will stimulate further modeling and experimental efforts to benchmark and refine the work presented. By expanding on the work of this study, extensions to complex interfacial systems, like those found in plasma medicine, can eventually be made to better understand important plasma applications. Further physical processes that should be considered in interfacial modeling may include electron solvation processes in polar liquids [11, 78], and condensed phase evaporation [74].

Acknowledgments

NG, GB, DC, and RW acknowledge the financial support from the Australian Government, through the Australian Postgraduate Award, James Cook University, through the HDR Research Enhancement Scheme, and the Australian Research Council, through its Discovery and DECRA schemes. IS and SD are supported by the Grants No. OI171037 and III41011 from the Ministry of Education, Science and Technological Development of the Republic of Serbia.

Appendix A. Input data at densities intermediate to the gas and liquid phases

In order accommodate $n_0(z)$ variation of input data, we have implemented an approximation method recently proposed, and benchmarked for simple atomic liquids, by Garland *et al* [75] that seeks to approximate input transport data and collision rates as weighted combinations of the gas and liquid extreme values. This process is analogous to Blanc's Law [79], or the energy-dependent approach proposed by Chiflikian [80], used for approximating transport data in gas mixtures, where instead we now seek to describe transport at intermediate densities between two density extremes of one substance instead of mixing two distinct gases. Where necessary to account for the differences in momentum transfer for gas and liquid systems, nonlinear weightings of gas and liquid extreme data are combined [75]. Using a zeroth order momentum transfer theory approximation [31, 75, 81], the nonlinear dependence is extracted via the angle-integrated structure factor evaluated at a given electron mean energy, $\langle\varepsilon\rangle$, and at a neutral atom density

$$s(\langle\varepsilon\rangle; n_0) = \frac{1}{2}\int_0^{\pi} S\left(\frac{2}{\hbar}\sqrt{2m_e\langle\varepsilon\rangle}\,\sin\frac{\chi}{2}; n_0\right)[1-\cos\chi]\mathrm{d}\chi \tag{A.1}$$

where, for this work, the static structure factor, $S\left(\frac{2}{\hbar}\sqrt{2m_e\langle\varepsilon\rangle}\,\sin\frac{\chi}{2}; n_0\right)$, is assumed to be the analytic Verlet–Weis corrected Percus–Yevick structure factor [47] which has been demonstrated to be a good approximation of atomic liquid structure [16, 29, 37, 82]. The full analytic expression is included in a preceding study [75]. When considering largely localized energy transfer due to inelastic excitations, we use simpler linear combinations of gas and liquid extrema data as this was demonstrated to provide a sufficient first-order approximation to the intermediate density's transport data because explicit modifications to the energy balance equation (9) are not required [30, 75].

A.1. Local field dependent input data

For the LFA model the drift velocity at intermediate densities, W_{int}, is approximated as function of reduced field, $\frac{E}{n_0}$. A weighted sum of reciprocals of gas, W_g, and liquid ,W_l, extreme values was used

$$\frac{1}{W_{\mathrm{int}}\left(\frac{E}{n_0}\right)} = x_g s_{\mathrm{int}}\left(\frac{E}{n_0}\right)\frac{1}{W_g\left(\frac{E}{n_0}\right)} + x_l\frac{s_{\mathrm{int}}\left(\frac{E}{n_0}\right)}{s_l\left(\frac{E}{n_0}\right)}\frac{1}{W_l\left(\frac{E}{n_0}\right)}, \tag{A.2}$$

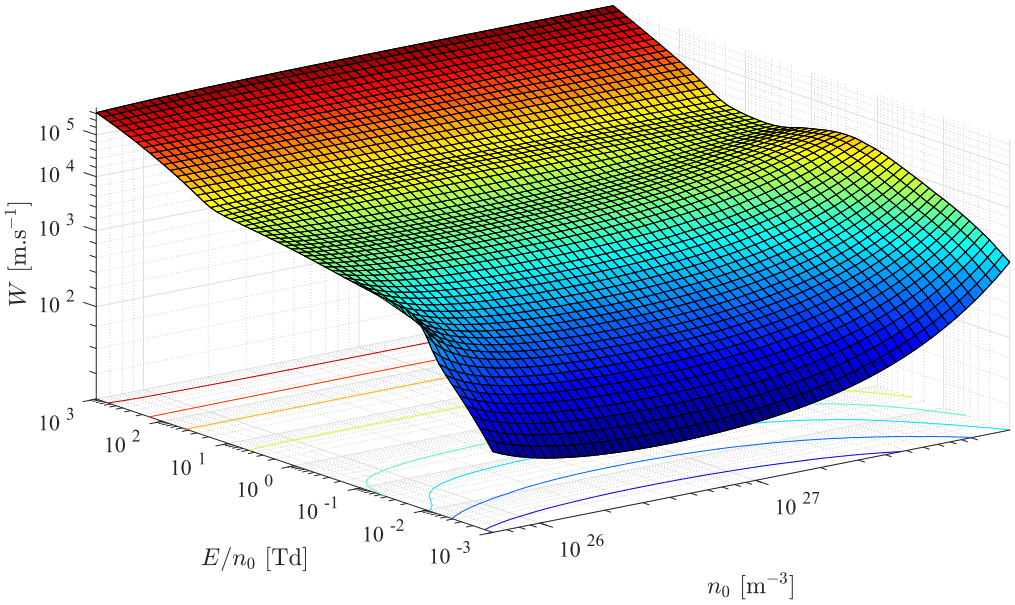

Figure A1. Drift velocity surface of electrons in argon as a function of $\frac{E}{n_0}$ and n_0 used to interpolate input data for LFA models.

where the density fractions, $x_{g,l}$, follow the relation

$$x_l = 1 - x_g. \tag{A.3}$$

These density fractions are determined by defining the intermediate density, n_{int}, as a sum of fractions of either density extrema

$$n_{\text{int}} = x_g n_g^{\text{eq}} + x_l n_l^{\text{eq}}, \tag{A.4}$$

and by combining (A.3) and (A.4) we find

$$x_g = \frac{n_l^{\text{eq}} - n_{\text{int}}}{n_l^{\text{eq}} - n_g^{\text{eq}}}. \tag{A.5}$$

The approximated angle-integrated structure factor at any intermediate points is given by

$$s_{\text{int}} \approx w s_g + (1 - w) s_l, \tag{A.6}$$

where s_g is defined as unity for the gas, s_l for the liquid extreme is evaluated via (A.1), and to ensure the approximation is physically grounded in both the high and low energy limits, the weighting factor, w, is fixed in the low energy limit by

$$w = \frac{S_{\text{int}}(0; n_{\text{int}}) - S_l(0; n_l)}{S_g(0; n_g) - S_l(0; n_l)}, \tag{A.7}$$

where $S(0; n)$ is the $\Delta k \to 0$ limit of the analytic structure factor [47], or otherwise proportional to the fluid compressibility which is a measurable input.

To demonstrate the output generated by this approximation method, we use (A.2) in conjunction with the accurate data of gas and liquid extremes described in section 2.2, to generate a drift velocity surface, shown in figure A1, which we interpolate onto as a function of the instantaneous $\frac{E}{n_0}$ and n_0 given at each point in space during the simulation.

We note that the reduced longitudinal diffusion coefficient $n_0 D_L$ was computed via a generalized Einstein relation [83] once the drift velocity was known via (A.2)

$$\frac{D_L^{\text{int}}}{\mu_{\text{int}}} = \frac{k_B T_0}{q}\left(1 + (1 + \Delta_{\text{int}})\frac{\partial \ln \mu_{\text{int}}}{\partial \ln E}\right), \tag{A.8}$$

where $\mu_{\text{int}} = \frac{W_{\text{int}}}{E}$ is the electron mobility derived from the drift velocity (A.2), T_0 is the neutral atom temperature, and the correction factor [83]

$$\Delta_{\text{int}} = \frac{\xi_{\text{int}}}{2 k_B T_0 W_{\text{int}}}, \tag{A.9}$$

where ξ_{int} is the electron heat flux which can be approximated via a similar rule as used for W_{int} via nonlinear combinations of gas, ξ_g, and liquid, ξ_l, extreme values

$$\frac{1}{\xi_{\text{int}}\left(\frac{E}{n_0}\right)} = x_g s_{\text{int}}\left(\frac{E}{n_0}\right)\frac{1}{\xi_g\left(\frac{E}{n_0}\right)} + x_l \frac{s_{\text{int}}\left(\frac{E}{n_0}\right)}{s_l\left(\frac{E}{n_0}\right)}\frac{1}{\xi_l\left(\frac{E}{n_0}\right)}. \tag{A.10}$$

A.2. Higher order model input data

The 4MM model collision data was also approximated between gas and liquid densities with energy dependent approximation methods [75]. As an example, as was done for the drift velocity, nonlinear weights taken from the angle-integrated structure factor are used to generate a sum rule using gas, $\check{\nu}_m^g$, and liquid, $\check{\nu}_m^l$, data to yield a reduced momentum transfer collision frequency at intermediate densities, $\check{\nu}_m^{\text{int}}$, evaluated at a common mean energy, $\langle\varepsilon\rangle$,

$$\check{\nu}_m^{\text{int}}(\langle\varepsilon\rangle) = x_g s_{\text{int}}(\langle\varepsilon\rangle)\check{\nu}_m^g(\langle\varepsilon\rangle) + x_l \frac{s_{\text{int}}(\langle\varepsilon\rangle)}{s_l(\langle\varepsilon\rangle)}\check{\nu}_m^l(\langle\varepsilon\rangle), \tag{A.11}$$

where $\check{\nu}$ notation is used to denote a reduced collision rate

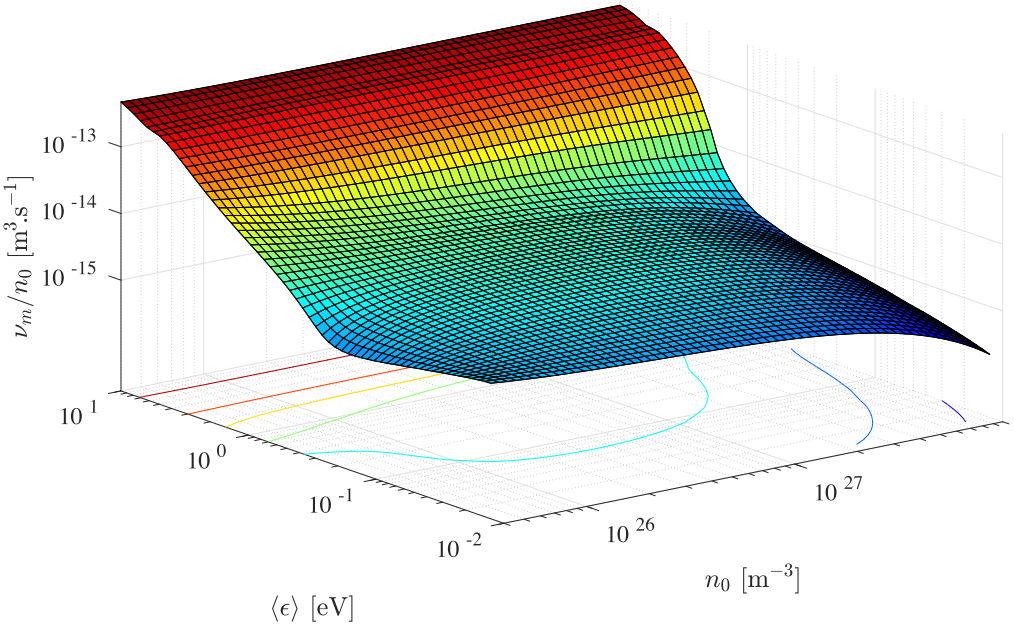

Figure A2. Reduced momentum transfer collision frequency, $\frac{\nu_m}{n_0}$, surface of electrons in argon computed via (A.11) as a function of $\langle\epsilon\rangle$ and n_0 used to interpolate input data for the 4MM model.

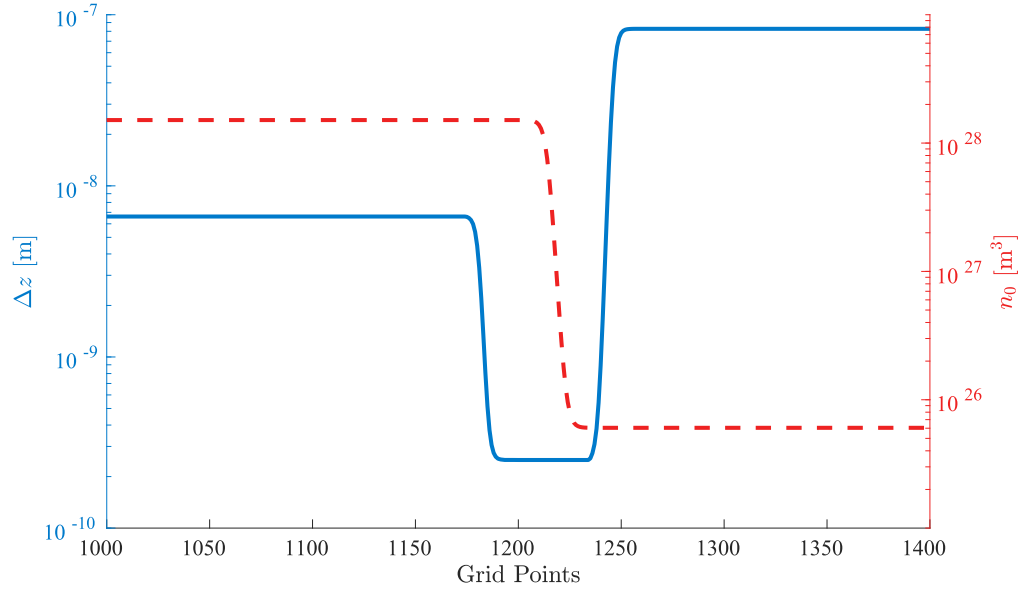

Figure B1. An example of the spatially varying numerical grid steps employed in discretization of the solution domain over the interface transition region.

scaled by n_0. To demonstrate the application of the nonlinear sum rule the reduced momentum transfer collision frequency surface generated via (A.11) is included in figure A2, demonstrating the reduction in momentum transfer collisions as the argon density increases.

Appendix B. Numerical solution of system of hyperbolic PDEs

Numerical solution of both the LFA and higher order fluid models for electron and ion properties was achieved by a custom flux-corrected transport (FCT) code [13], with explicit fourth order Runge–Kutta (RK4) time-integration used to advance forward in time [84–86]. Spatial discretization was performed via FCT by augmenting a monotonic first order upwinding scheme [87], with a second order conservative finite difference scheme. The FCT flux limiting algorithm of Boris and Book [85, 86] was used to enable resolution of sharp gradients found in ionization fronts. To account for the varying length scales present in the problems, we employed variably spaced grids, as shown in figure B1, to allow spatial steps appropriate to liquid, gas, and interfacial regions. Given the spatial grid sizes, time step size was chosen as the smallest

step computed via: (i) a Courant–Friedrichs–Lewy (CFL) condition of 0.05, or (ii) 1/20 of the fastest collisional relaxation time. Employing both the spatial discretization of FCT and RK4 time-integration assists in avoiding excessive numerical diffusion that may be introduced as a result of small time steps due to the small CFL number.

Solution of the coupled electric field evolution was obtained via second order finite difference discretization of (3) and (4), given fixed boundary conditions for electric potential at either end of the solution domain [13]. To ensure the accuracy of this scheme, systematic benchmarking was performed by comparing numerical solutions against known analytic solutions, and ensuring particle conservation was guaranteed at each time step. Typical systems used for benchmarking are square-wave advection, Gaussian pulse advection-diffusion, and the solution of Euler's equations for Sod's shock-tube [84–86].

Continuous boundary conditions were implemented to allow passage of information outside of the solution domain to avoid impacting the solution. To further assist in this aim, streamer formation and propagation was performed well inside the solution domain, away from the necessary boundaries, to minimize the impact of boundary conditions.

ORCID iDs

N A Garland https://orcid.org/0000-0003-0343-0199
G J Boyle https://orcid.org/0000-0002-8581-4307
D G Cocks https://orcid.org/0000-0002-9943-7100
R D White https://orcid.org/0000-0001-5353-7440

References

[1] Economou D J 2014 Pulsed plasma etching for semiconductor manufacturing *J. Phys. D: Appl. Phys.* **47** 303001
[2] Boeuf J P and Pitchford L C 1995 Two-dimensional model of a capacitively coupled rf discharge and comparisons with experiments in the Gaseous Electronics Conference reference reactor *Phys. Rev.* E **51** 1376–90
[3] Lymberopoulos D P and Economou D J 1995 Two-dimensional self-consistent radio-frequency plasma simulations relevant to the gaseous electronics conference rf reference cell *J. Res. Natl Inst. Stand. Technol.* **100** 473
[4] Dujko S, Markosyan A H, White R D and Ebert U 2013 High-order fluid model for streamer discharges: I. Derivation of model and transport data *J. Phys. D: Appl. Phys.* **46** 475202
[5] Morrow R and Lowke J J 1997 Streamer propagation in air *J. Phys. D: Appl. Phys.* **30** 614–27
[6] Qin J, Pasko V P, McHarg M G and Stenbaek-Nielsen H C 2014 Plasma irregularities in the d-region ionosphere in association with sprite streamer initiation *Nat. Commun.* **5** 1–6
[7] Marinov I, Starikovskaia S and Rousseau A 2014 Dynamics of plasma evolution in a nanosecond underwater discharge *J. Phys. D: Appl. Phys.* **47** 224017
[8] Akishev Y, Karalnik V, Medvedev M, Petryakov A, Shafikov A and Trushkin N 2017 Propagation of positive streamers on the surface of shallow as well as deep tap water in wide and narrow dielectric channels *Plasma Sources Sci. Technol.* **26** 025004
[9] Lindsay A D, Graves D B and Shannon S C 2016 Fully coupled simulation of the plasma liquid interface and interfacial coefficient effects *J. Phys. D: Appl. Phys.* **49** 235204
[10] Bruggeman P J *et al* 2016 Plasma-liquid interactions: a review and roadmap *Plasma Sources Sci. Technol.* **25** 053002
[11] Mariotti D, Patel J, Švrček V and Maguire P 2012 Plasma-liquid interactions at atmospheric pressure for nanomaterials synthesis and surface engineering *Plasma Process. Polym.* **9** 1074–85
[12] Richmonds C, Witzke M, Bartling B, Lee S W, Wainright J, Liu C C and Sankaran R M 2011 Electron-transfer reactions at the plasma-liquid interface *J. Am. Chem. Soc.* **133** 17582–5
[13] Garland N A, Cocks D G, Boyle G J, Dujko S and White R D 2017 Unified fluid model analysis and benchmark study for electron transport in gas and liquid analogs *Plasma Sources Sci. Technol.* **26** 075003
[14] Becker M M, Kählert H, Sun A, Bonitz M and Loffhagen D 2017 Advanced fluid modeling and PIC/MCC simulations of low-pressure ccrf discharges *Plasma Sources Sci. Technol.* **26** 044001
[15] Markosyan A H, Teunissen J, Dujko S and Ebert U 2015 Comparing plasma fluid models of different order for 1D streamer ionization fronts *Plasma Sources Sci. Technol.* **24** 065002
[16] Boyle G J, McEachran R P, Cocks D G and White R D 2015 Electron scattering and transport in liquid argon *J. Chem. Phys.* **142** 154507
[17] Boyle G J, Tattersall W J, Cocks D G, McEachran R P and White R D 2017 A multi-term solution of the space–time Boltzmann equation for electrons in gases and liquids *Plasma Sources Sci. Technol.* **26** 024007
[18] Akimov D, Bondar A, Burenkov A and Buzulutskov A 2009 Detection of reactor antineutrino coherent scattering off nuclei with a two-phase noble gas detector *J. Instrum.* **4** P06010
[19] Bondar A, Buzulutskov A, Grebenuk A, Pavlyuchenko D, Snopkov R and Tikhonov Y 2006 Two-phase argon and xenon avalanche detectors based on Gas Electron Multipliers *Nucl. Instrum. Methods Phys. Res.* A **556** 273–80
[20] Brunetti R *et al* 2005 WARP liquid argon detector for dark matter survey *New Astron. Rev.* **49** 265–9
[21] Sangiorgio S *et al* 2013 First demonstration of a sub-keV electron recoil energy threshold in a liquid argon ionization chamber *Nucl. Instrum. Methods Phys. Res.* A **728** 69–72
[22] Regenfus C 2010 The argon dark matter experiment (ArDM) *J. Phys.: Conf. Ser.* **203** 99–102
[23] Adamovich I *et al* 2017 The 2017 Plasma Roadmap: Low temperature plasma science and technology *J. Phys. D: Appl. Phys.* **50** 323001
[24] Babaeva N Y, Tian W and Kushner M J 2014 The interaction between plasma filaments in dielectric barrier discharges and liquid covered wounds: electric fields delivered to model platelets and cells *J. Phys. D: Appl. Phys.* **47** 235201
[25] Bruggeman P and Leys C 2009 Non-thermal plasmas in and in contact with liquids *J. Phys. D: Appl. Phys.* **42** 053001
[26] Gopalakrishnan R, Kawamura E, Lichtenberg A J, Lieberman M A and Graves D B 2016 Solvated electrons at the atmospheric pressure plasma-water anodic interface *J. Phys. D: Appl. Phys.* **49** 295205
[27] Lietz A M and Kushner M J 2016 Air plasma treatment of liquid covered tissue: long timescale chemistry *J. Phys. D: Appl. Phys.* **49** 425204
[28] Tian W and Kushner M J 2014 Atmospheric pressure dielectric barrier discharges interacting with liquid covered tissue *J. Phys. D: Appl. Phys.* **47** 165201

[29] Boyle G J, McEachran R P, Cocks D G, Brunger M J, Buckman S J, Dujko S and White R D 2016 *Ab initio* electron scattering cross-sections and transport in liquid xenon *J. Phys. D: Appl. Phys.* **49** 355201

[30] White R D and Robson R E 2011 Multiterm solution of a generalized Boltzmann kinetic equation for electron and positron transport in structured and soft condensed matter *Phys. Rev.* E **84** 031125

[31] Robson R, White R and Hildebrandt M 2017 *Fundamentals of Charged Particle Transport in Gases and Condensed Matter (Monograph Series in Physical Sciences)* (Boca Raton, FL: CRC Press)

[32] Hagelaar G J M and Kroesen G M W 2000 Speeding up fluid models for gas discharges by implicit treatment of the electron energy source term *J. Comput. Phys.* **159** 1–12

[33] Ebert U *et al* 2011 Multiple scales in streamer discharges, with an emphasis on moving boundary approximations *Nonlinearity* **24** C1–26

[34] Meunier J, Belenguer P and Boeuf J P 1995 Numerical-model of an Ac plasma display panel cell in neon-xenon mixtures *J. Appl. Phys.* **78** 731–45

[35] Becker M M and Loffhagen D 2013 Derivation of moment equations for the theoretical description of electrons in nonthermal plasmas *Adv. Pure Math.* **03** 343–52

[36] Robson R E, White R D and Petrović Z L 2005 Colloquium : Physically based fluid modeling of collisionally dominated low-temperature plasmas *Rev. Mod. Phys.* **77** 1303–20

[37] Tattersall W J, Cocks D G, Boyle G J, Buckman S J and White R D 2015 Monte Carlo study of coherent scattering effects of low-energy charged particle transport in Percus–Yevick liquids *Phys. Rev.* E **91** 043304

[38] Dujko S, White R D, Petrović Z L and Robson R E 2010 Benchmark calculations of nonconservative charged-particle swarms in dc electric and magnetic fields crossed at arbitrary angles *Phys. Rev.* E **81** 046403

[39] Birdsall C K 1991 Particle-in-cell charged-particle simulations, plus Monte Carlo collision with neutral atom, PIC-MCC *IEEE Trans. Plasma Sci.* **19** 65–85

[40] Robson R E, Nicoletopoulos P, Hildebrandt M and White R D 2012 Fundamental issues in fluid modeling: direct substitution and aliasing methods *J. Chem. Phys.* **137** 214112

[41] Turner M M, Derzsi A, Donkó Z, Eremin D, Kelly S J, Lafleur T and Mussenbrock T 2013 Simulation benchmarks for low-pressure plasmas: capacitive discharges *Phys. Plasmas* **20** 013507

[42] Becker M M and Loffhagen D 2013 Enhanced reliability of drift-diffusion approximation for electrons in fluid models for nonthermal plasmas *AIP Adv.* **3** 012108

[43] Dujko S, White R D and Petrović Z L 2008 Monte Carlo studies of non-conservative electron transport in the steady-state Townsend experiment *J. Phys. D: Appl. Phys.* **41** 245205

[44] White R D, Robson R E, Dujko S, Nicoletopoulos P and Li B 2009 Recent advances in the application of Boltzmann equation and fluid equation methods to charged particle transport in non-equilibrium plasmas *J. Phys. D: Appl. Phys.* **42** 194001

[45] Phelps A V 1991 Cross sections and swarm coefficients for nitrogen ions and neutrals in N_2 and argon ions and neutrals in Ar for energies from 0.1 eV to 10 keV *J. Phys. Chem. Ref. Data* **20** 557–73

[46] Viehland L A and Kirkpatrick C C 1995 Relating ion/neutral reaction rate coefficients and cross-sections by accessing a database for ion transport properties *Int. J. Mass Spectrom. Ion Process.* **149–150** 555–71

[47] Verlet L and Weis J-J 1972 Equilibrium theory of simple liquids *Phys. Rev.* A **5** 939–52

[48] Markosyan A H, Dujko S and Ebert U 2013 High-order fluid model for streamer discharges: II. Numerical solution and investigation of planar fronts *J. Phys. D: Appl. Phys.* **46** 475203

[49] Grubert G K, Becker M M and Loffhagen D 2009 Why the local-mean-energy approximation should be used in hydrodynamic plasma descriptions instead of the local-field approximation *Phys. Rev.* E **80** 036405

[50] Biondi M A and Brown S C 1949 Measurement of electron–ion recombination *Phys. Rev.* **76** 1697–700

[51] Foxe M, Hagmann C, Jovanovic I, Bernstein A, Kazkaz K, Mozin V, Pereverzev S V, Sangiorgio S and Sorensen P 2015 Low-energy (<10 keV) electron ionization and recombination model for a liquid argon detector *Nucl. Instrum. Methods Phys. Res.* A **771** 88–92

[52] Kubota S, Nakamoto A, Takahashi T, Hamada T, Shibamura E, Miyajima M, Masuda K and Doke T 1978 Recombination luminescence in liquid argon and in liquid xenon *Phys. Rev.* B **17** 2762–5

[53] Shinsaka K, Codama M, Srithanratana T, Yamamoto M and Hatano Y 1988 Electron–ion recombination rate constants in gaseous, liquid, and solid argon *J. Chem. Phys.* **88** 7529–36

[54] Thomas J and Imel D A 1987 Recombination of electron–ion pairs in liquid argon and liquid xenon *Phys. Rev.* A **36** 614–6

[55] Hayashi M 2003 *Bibliography of Electron and Photon Cross Sections With Atoms and Molecules Published in the 20th Century—Argon Report* NIFS-DATA-72 National Institute for Fusion Science of Japan

[56] Hayashi Database. www.lxcat.net, (Retrieved: 18 February 2018)

[57] Dujko S, Simonovic I, Boyle G, White R, Bosnjakovic D and Petrovic Z 2016 Transport properties of electrons and transition of an electron avalanche into a streamer in atomic liquids *APS Gaseous Electronics Conf. 2016 Abstracts* p MW6.036

[58] Simonović I, Petrović Z L and Dujko S 2017 Simulation of electron transport and negative planar streamer fronts in liquid argon anf liquid xenon *Proc. 21st Symp. on Application of Plasma Processes (SAPP XXI)* pp 226–30

[59] Schmidt W F and Illenberger E 2003 Low energy electrons in non-polar liquids *Nukleonika* **48** 75–82

[60] Evans C M and Findley G L 2010 Energy of the conduction band in near critical point fluids *Phys. Res. Int.* **2010** 1–6

[61] Asaf U and Steinberger I T 1974 Photoconductivity and electron transport parameters in liquid and solid xenon *Phys. Rev.* B **10** 4464–8

[62] Miyajima M, Takahashi T, Konno S, Hamada T, Kubota S, Shibamura H and Doke T 1974 Average energy expended per ion pair in liquid argon *Phys. Rev.* A **9** 1438–43

[63] Laporte P, Subtil J L, Reininger R, Saile V, Bernstorff S and Steinberger I T 1987 Evolution of intermediate excitons in fluid argon and krypton *Phys. Rev.* B **35** 6270–80

[64] Laporte P and Steinberger I T 1977 Evolution of excitonic bands in fluid xenon *Phys. Rev.* A **15** 2538–44

[65] Laporte P, Subtil J L, Asaf U, Steinberger I T and Wind S 1980 Intermediate and wannier excitons in fluid xenon *Phys. Rev. Lett.* **45** 2138–40

[66] Haensel R, Keitel G, Koch E E, Skibowski M and Schreiber P 1969 Reflection spectrum of solid argon in the vacuum ultraviolet *Phys. Rev. Lett.* **23** 1160–3

[67] Gushchin E M, Kruglov A A and Obodovskii I M 1982 Electron dynamics in condensed argon and xenon *Sov. Phys.—JETP* **55** 650–5

[68] Kalos M H, Percus J K and Rao M 1977 Structure of a liquid–vapor interface *J. Stat. Phys.* **17** 111–36

[69] Halpern B, Lekner J, Rice S and Gomer R 1967 Drift velocity and energy of electrons in liquid argon *Phys. Rev.* **156** 351–2

[70] Lee D J, Telo Da Gama M M and Gubbins K E 1984 The vapour–liquid interface for a Lennard-Jones model of argon-krypton mixtures *Mol. Phys.* **53** 1113–30
[71] Trokhymchuk A and Alejandre J 1999 Computer simulations of liquid/vapor interface in Lennard-Jones fluids: some questions and answers *J. Chem. Phys.* **111** 8510–23
[72] Yi P, Poulikakos D, Walther J and Yadigaroglu G 2002 Molecular dynamics simulation of vaporization of an ultra-thin liquid argon layer on a surface *Int. J. Heat Mass Transfer* **45** 2087–100
[73] Chapela G A, Saville G, Thompson S M and Rowlinson J S 1977 Computer simulation of a gsa–liquid surface: I *J. Chem. Soc. Faraday Trans.* II **73** 1133–44
[74] Ishiyama T, Yano T and Fujikawa S 2004 Molecular dynamics study of kinetic boundary condition at an interface between argon vapor and its condensed phase *Phys. Fluids* **16** 2899–906
[75] Garland N A, Boyle G J, Cocks D G and White R D 2018 Approximating the nonlinear density dependence of electron transport coefficients and scattering rates across the gas–liquid interface *Plasma Sources Sci. Technol.* **27** 024002
[76] Amey R L and Cole R H 1964 Dielectric constants of liquefied noble gases and methane *J. Chem. Phys.* **40** 146–8
[77] Lippold H 1969 Isothermal compressibility and density of liquid argon and neon up to pressures of 1000 $\mathrm{kg/cm^2}$ *Cryogenics* **9** 112–4
[78] Abel B, Buck U, Sobolewski A L and Domcke W 2012 On the nature and signatures of the solvated electron in water *Phys. Chem. Chem. Phys.* **14** 22–34
[79] Blanc A 1908 Recherches sur les mobilités des ions dans les gaz *J. Phys. Théor. Appl.* **7** 825–39
[80] Chiflikian R V 1995 The analog of Blanc's law for drift velocities of electrons in gas mixtures in weakly ionized plasma *Phys. Plasmas* **2** 3902–9
[81] Boyle G J, White R D, Robson R E, Dujko S and Lj Petrović Z 2012 On the approximation of transport properties in structured materials using momentum-transfer theory *New J. Phys.* **14** 045011
[82] Lekner J 1967 Motion of electrons in liquid argon *Phys. Rev.* **158** 130–7
[83] Robson R E 1984 Generalized einstein relation and negative differential conductivity in gases *Aust. J. Phys.* **37** 35
[84] Zalesak S T 2012 The design of flux-corrected transport (FCT) algorithms for structured grids *Flux-Corrected Transport* (*Scientific Computation*) ed D Kuzmin *et al* 1 edn (Dordrecht: Springer) ch 2, pp 23–65
[85] Boris J P and Book D L 1973 Flux-corrected transport: I. SHASTA, a fluid transport algorithm that works *J. Comput. Phys.* **11** 38–69
[86] Zalesak S T 1979 Fully multidimensional flux-corrected transport algorithms for fluids *J. Comput. Phys.* **31** 335–62
[87] Swanson R C and Turkel E 1992 On central-difference and upwind schemes *J. Comput. Phys.* **101** 292–306